

Multi-head Cascaded Swin Transformers with Attention to k-space Sampling Pattern for Accelerated MRI Reconstruction

Mevan Ekanayake^{a,b,1}, Kamlesh Pawar^a, Mehrtash Harandi^b, Gary Egan^{a,c}, and Zhaolin Chen^{a,d}

^a*Monash Biomedical Imaging, Monash University, Clayton, VIC 3800 Australia*

^b*Department of Electrical and Computer Systems Engineering, Monash University, Clayton, VIC 3800 Australia*

^c*School of Psychological Sciences, Monash University, Clayton, VIC 3800 Australia*

^d*Department of Data Science and AI, Monash University, Clayton, VIC 3800 Australia*

Abstract

Global correlations are widely seen in human anatomical structures due to similarity across tissues and bones. These correlations are reflected in magnetic resonance imaging (MRI) scans as a result of close-range proton density and T1/T2 parameter. Furthermore, to achieve accelerated MRI, k-space data are undersampled which causes global aliasing artefacts. Convolutional neural network (CNN) models are widely utilized for accelerated MRI reconstruction, but those models are limited in capturing global correlations due to the intrinsic locality of the convolution operation. The self-attention-based transformer models are capable of capturing global correlations among image features, however, the current contributions of transformer models for MRI reconstruction are minute. The existing contributions mostly provide CNN-transformer hybrid solutions and rarely leverage the physics of MRI. In this paper, we propose a physics-based stand-alone (convolution free) transformer model titled, the Multi-head Cascaded Swin Transformers (McSTRA) for accelerated MRI reconstruction. McSTRA combines several interconnected MRI physics-related concepts with the transformer networks: it exploits global MR features via the shifted window self-attention mechanism; it extracts MR features belonging to different spectral components separately using a multi-head setup; it iterates between intermediate de-aliasing and k-space correction via a cascaded network with data consistency in k-space and intermediate loss computations; furthermore, we propose a novel positional embedding generation mechanism to guide self-attention utilizing the point spread function corresponding to the undersampling mask. Our model significantly outperforms state-of-the-art MRI reconstruction methods both visually and quantitatively while depicting improved resolution and removal of aliasing artifacts. Further experiments demonstrate the superior capabilities of McSTRA in combating adversarial conditions such as higher accelerations, noisy data, different undersampling protocols, out-of-distribution data, and abnormalities in anatomy.

Keywords: accelerated MRI, deep learning, image reconstruction, point spread function, Swin transformer, undersample, k-space

¹Corresponding author.

E-mail address: mevan.ekanayake@monash.edu

1 Introduction

The outstanding soft tissue contrast and flexibility make magnetic resonance imaging (MRI) a comprehensive diagnostic tool for a broad range of disorders, including musculoskeletal, neurological, and oncological diseases. Compared with other modalities, MRI is unique in producing non-invasive measures for imaging anatomy, diffusion process, and functions in the human body (Nishimura, 1996). However, the long data acquisition time is a significant issue in MRI, which leads to patient discomfort, image artifacts, and high examination costs (Zbontar et al., 2019). Image reconstruction in MRI is an inverse process that reconstructs images with diagnostic quality from acquired MR data (or k-space). A trade-off between image quality and acquisition time is often made by undersampling the k-space to accelerate the data acquisition process, which is commonly known as accelerated MRI reconstruction.

Undersampling the k-space violates the Nyquist-Shannon sampling theorem thereby introducing aliasing artifacts. These artifacts must be eliminated during the course of the image reconstruction process. Early solutions involved linear analytic methods such as partial Fourier encoding, sensitivity encoding (SENSE) (Pruessmann et al., 1999), simultaneous acquisition of spatial harmonics (SMASH) (Sodickson and Manning, 1997), and generalized auto calibrating partially parallel acquisitions (GRAPPA) (Griswold et al., 2002), which incorporates prior knowledge of the imaging systems as well as k-space correlations. Later, the reconstruction methodologies drifted toward solving optimization problems using non-linear iterative algorithms which incorporated physics of the imaging system and as well as regularization of priors such as sparsity (Chaâri et al., 2011), low rank (Haldar and Zhuo, 2016), manifold (Wachinger et al., 2012), total variation (Block et al., 2007), and dictionary learning (Weller, 2016). However, these methods are limited in both model capacity and model parameter tuning, hence offering inadequate flexibility resulting in suboptimal performance.

Driven by the explosion in artificial intelligence, deep learning (DL) methods have shown promising results for accelerated MRI reconstruction (Hammernik et al., 2018; Wang et al., 2016; Zhu et al., 2018) due to their flexibility and capacity. These methods are capable of learning complex patterns from a large amount of training data. Many DL-based MRI reconstruction methods are subsequently developed using convolutional neural network (CNN) models which can be studied under two main categories (Wang et al., 2021), i.e. data-driven end-to-end DL methods which map the low-quality undersampled images to high-quality references (Hyun et al., 2018; Pawar et al., 2021, 2019; Wang et al., 2016; Yang et al., 2018) and physics-constrained DL methods which iteratively solve for an inverse problem (Aggarwal et al., 2019; Schlemper et al., 2018; yang et al., 2016).

Global correlations are often observed in human anatomical structures as a result of the similarity across different tissues and bones. These are reflected in MRI scans as a result of close-range proton density and T1/T2 parameters and in a random undersampling setting, the aliasing artifacts have an in-coherent appearance which causes global correlations in the image space. As a result, exploiting global correlations could be highly beneficial in accomplishing improved image quality in MRI such as in the denoising application using non-local means filtering (Manjón et al., 2008) and BM3D filtering (Dabov et al., 2006). The CNN models are suboptimal in capturing these global image correlations due to the intrinsic locality of the convolution operation caused by the narrow receptive fields of the CNN kernels. This issue could be mitigated by stacking more CNN layers sequentially but that would increase the computational burden and the amount of training required.

The transformer models have recently shown significant improvement in capturing global correlations via the inherent self-attention mechanism in many natural language processing (NLP) and computer vision (CV) tasks. With respect to CV-based applications, the image is simply divided into patches; the patches are converted into vectorized tokens; and the tokens are subjected to self-attention. This strategy not only saves the computational burden but also aggregates global correlations of the entire image at once, rather than confining to local kernels. Despite the rapid success, the current applications of transformer models for accelerated MRI reconstruction are minute and suboptimal. There are several preliminary works (Feng et al., 2021; Huang et al., 2022; Korkmaz et al., 2022, 2021; Yan et al., 2021) combining CNN layers with transformer models, but those methods have not incorporated MRI physics or the imaging system, hence limited in performance.

In this paper, we aim to develop a novel physics-based transformer model referred to as McSTRA (stands for Multi-head Cascaded Swin Transformers) for accelerated MRI reconstruction by combining several interlinked physics-based strategies. Our model is free of CNN layers and to the best of our knowledge, the first study to utilize the Swin-Unet (Cao et al., 2021) incorporated physics knowledge for accelerated MRI reconstruction. The Swin-Unet model hierarchically extracts features at different spatial resolutions while incorporating the shifted window self-attention mechanism allowing accurate reconstruction of global features in all resolution levels. First, McSTRA extracts MR features belonging to different spectral components by decomposing the k-space into low-frequency features (corresponding to anatomical and structural information) and high-frequency features (corresponding to edge features and resolution information) and reconstructing them separately using a multi-head setup. Then, it iterates between intermediate de-aliasing and k-space correction via a cascaded network with data consistency (DC) in k-space and intermediate loss computations in order to incrementally reconstruct images. Finally, it performs an image-to-image mapping in order to reconstruct the final magnitude MR image. We also propose a novel positional embedding generation mechanism to guide self-attention layers within the transformer models. This mechanism exploits the relationship between the point spread function (PSF) of the sampling protocol and the pattern of the aliasing artifacts within the field of view to generate an instant dependent positional embedding. In this study, we comprehensively evaluate the performance of McSTRA in combating adversarial conditions such as higher accelerations, noisy data, different undersampling protocols, out-of-distribution data, and abnormalities in anatomy.

The remainder of the paper is arranged as follows. Section 2 describes the literature related to the underlying concepts of McSTRA. Section 3 presents several theoretical formulations to support the functionality of the constituent components of McSTRA. In Section 4, the novel McSTRA model is introduced. Section 5 shows empirical results, including quantitative and qualitative evaluations on the large-scale fastMRI dataset followed by ablation studies to comprehend the behavior of McSTRA. Section 6 summarizes the paper and describes the limitations of our work along with the future directions.

2 Related Work

This Section summarizes the previous works that align with the underlying concepts of McSTRA.

Cascaded Deep Learning Models for MRI Reconstruction. Several previous works proposed DL models for MRI reconstruction that consist of cascaded CNN blocks and DC blocks that perform k-space correction (Schlemper et al., 2018; Souza et al., 2019; Zheng et al., 2019). In Schlemper et al. (2017, 2018), a cascaded DL model consisting of CNN layers was proposed for accelerated MRI reconstruction in cardiac MR. The cascaded network consists of CNN models interleaved with DC layers and data sharing layers where the data sharing layers are utilized for dynamic sequences. The underlying principle of the cascaded network is to iterate between the intermediate de-aliasing and k-space correction. The 2D slice reconstruction in this study showed considerable improvement in reconstruction over the traditional compressed sensing methods. Zheng et al. (2019) proposed a Cascaded Dilated Dense Network (CDDN) for MRI reconstruction which contains multiple sub-network iterations and after each sub-network, a two-step data consistency (TDC) is performed on the k-space. The experiments were conducted on the cardiac dataset and the fastMRI dataset where significant improvements were observed. Apart from that, Kocanaogullari and Eksioglu (2019), and Souza et al. (2019) also adopted the cascaded structure in DL setting for MRI reconstruction.

Transformers. Self-attention-based transformer models which exploit the global correlations in data have shown massive improvement in NLP tasks such as machine translation, text classification, and visual question answering (Galassi et al., 2021; Vaswani et al., 2017). Following this success, the CV community has shown considerable interest in adopting transformer models for various vision tasks over the last couple of years. For example, Google Research introduced the Vision Transformer (ViT) which was able to outperform all the state-of-the-art CNN-based models in image classification (Dosovitskiy et al., 2021).

The recent Swin transformer (Liu et al., 2021) was able to outperform many state-of-the-art methods in image segmentation and object detection. The Swin transformer is a transformer variant which not only operates on image patches but also models global correlations via a shifted window mechanism (See Fig. 1(c)). This type of partitioning mechanism will enable the model to capture global correlations for an effective reconstruction. Several transformer models such as Swin-Unet (Cao et al., 2021), TransUNet (Chen et al., 2021), and Medical Transformer (Valanarasu et al., 2021) have been proposed specifically to solve medical image analysis tasks such as segmentation and detection. Swin-Unet is an Unet-like pure transformer network proposed for medical image segmentation. Similar to the conventional U-Net architecture, Swin-Unet consists of an encoder, a bottleneck, and a decoder containing several Swin transformer blocks as can be seen in Fig. 3(c).

Transformer-based MRI Reconstruction. Recently, there have been some transformer-based DL models proposed for MRI reconstruction. The SwinMRI model (Huang et al., 2022) couples parallel imaging with the Swin transformer for multi-channel MRI reconstruction. Their experiments on Calgary Campinas multi-channel brain dataset and the Multi-modal Brain Tumor Segmentation Challenge 2017 (BraTS17) dataset demonstrated superior performance over CNN-based and GAN-based MRI reconstruction methods. SwinMRI also showed excellent robustness to various undersampling trajectories and noise levels.

Korkmaz et al. (2022, 2021) proposed unsupervised learning-based transformer models for MRI reconstruction. Their work centered around deep image prior (DIP) and adversarial learning. The DIP-based model (Korkmaz et al., 2021) referred to as GVTrans progressively maps low-dimensional noise and latent variables onto MR images via cascaded blocks of cross-attention ViTs. The adversarial learning-based method (Korkmaz et al., 2022) referred to as SLATER, embodies a deep adversarial network with cross-attention transformers to map noise and latent variables onto coil-combined MR images. Their experiment on the IXI brain dataset and the fastMRI brain dataset showed improved image quality compared to CNN-based reconstructions.

Several works proposed transformer-based models for joint MRI reconstruction and super-resolution. Feng et al. (2021) focused on multi-task learning which involves sharing structural information between higher-quality and super-resolved reconstructions and their experiments on the IXI brain MRI dataset showed reduced blurring and artifacts. Yan et al. (2021) proposed a Swin transformer-based model referred to as SMIR which focuses on two simultaneous tasks: multi-level feature extraction and image reconstruction. SMIR incorporates both spatial and frequency domain losses and their experiments display improved performance under a wide range of acceleration factors on the HCP brain dataset.

Feng et al. (2022) proposed a unified transformer framework referred to as MTrans for multi-modal MR imaging. MTrans utilizes a cross attention module, which extracts and transfers features from an auxiliary modality to a target modality. Their experiments on fastMRI knee and brain MRI datasets validate improved reconstruction performance.

Positional Embeddings. Transformer networks are fundamentally built up on the concept of multi-head self-attention. This self-attention operation in transformers unlike CNNs involves fully connected layers, hence permutation-invariant, i.e., it does not have awareness of the order of the input token sequence. This could harm the learning process of transformers, especially in the image domain since the order of the sequence is important for capturing its content. In order to incorporate the order of sequence, initial works proposed fixed positional embeddings (Vaswani et al., 2017) with sinusoidal functions and learnable positional embeddings (Dosovitskiy et al., 2021) that were added to input features before subjecting to the self-attention operation.

Several learnable positional embedding strategies were proposed in Dosovitskiy et al. (2021) such as 1-dimensional positional embedding, 2-dimensional positional embedding, and relative positional embedding (also discussed in Shaw et al. (2018)). Influenced by the success of incorporating positional embeddings, several other variants were proposed later. In Liu et al. (2020), an efficient position encoding scheme called FLOATER was introduced where position information was modeled with a continuous dynamical model. In Chu et al. (2021), a conditional positional embedding strategy was introduced where a position encoding generator produces positional embeddings conditioned on the input.

Decomposition of k-space. The k-space signals are well known to be non-uniformly distributed in terms of spectral energy, i.e., the magnitude tends to be larger in low-frequency bands (or center region) and contains more anatomical and structural information whereas the magnitude is small in high-frequency bands (or the outer region) and contains edge features and resolution information (Nguyen-Duc et al., 2019; Wu et al., 2016). Nevertheless, the high-frequency bands contain diagnostically important information (He et al., 2019). Many DL-based models enforce a uniform loss function over the entire field of view and k-space which results in imbalance training for the high

frequencies in k-space due to their intrinsic low magnitude. Such imbalance can cause further loss of resolution.

Improved characterization of k-space has demonstrated improved accuracy in MRI reconstruction, e.g., compressed sensing MRI (Nguyen-Duc et al., 2019; Sung and Hargreaves, 2013; Yang et al., 2015), spread spectrum MRI (Pawar et al., 2020, 2015), self-supervision (Yaman et al., 2020).

Further, The study by Sun et al. (2019) explicitly demonstrated the significance of sustaining high-frequency k-space information where the authors propose a subspace decomposition approach which is accomplished by using complementary filter banks referred to as HoriVert. The images are reconstructed in complementary subspaces belonging to high- and low-frequency decomposition in k-space individually using off-the-shelf algorithms, and finally fused together to obtain the final reconstruction. Similar approaches have been adopted in several other works (Faris, 2021; Faris et al., 2021; He et al., 2019).

3 Theory

This Section provides several theoretical formulations which we utilize to support the functionality of the constituent components of McSTRA. Throughout the remainder of the paper, we utilize the variable \mathbf{x} and its variants to denote MR data in image space, the variable \mathbf{y} and its variants to denote MR data in k-space, and the variable \mathbf{z} and its variants to denote intermediate latent MR features.

3.1 MRI Reconstruction

Let $\mathbf{x} \in \mathbb{C}^N$ be the complex-valued vector representation of an MR image and $\mathbf{y} \in \mathbb{C}^N$ be the fully sampled measurements in k-space. Then, the forward model of MRI acquisition can be presented as $\mathbf{y} = \mathbf{F}\mathbf{x}$, where $\mathbf{F} \in \mathbb{C}^{N \times N}$ denotes the Fourier encoding matrix. Thus, in a fully sampled scenario, a clean MR image as seen in Fig. 1(a) can be reconstructed by $\mathbf{x} = \mathbf{F}^H\mathbf{y}$, where \mathbf{F}^H is the inverse Fourier encoding matrix. Note that the above represents single channel (or channel combined) data acquisition whereas, in multi-channel data acquisition, a coil sensitivity matrix should be included. Accelerated MRI can be achieved by sampling only a subset of k-space samples, $\hat{\mathbf{y}}$. This is usually modelled using a binary sampling mask, $\mathbf{M} \in \{0,1\}^N$ i.e., $\hat{\mathbf{y}} = \mathbf{M} \odot \mathbf{y}$, where \mathbf{M} takes a value of 1 at locations where the k-space is sampled and 0 elsewhere, and \odot represents the Hadamard product. However, a directly reconstructed image, $\hat{\mathbf{x}} = \mathbf{F}^H\hat{\mathbf{y}}$ will have global aliasing artifacts as seen in Fig. 1(b).

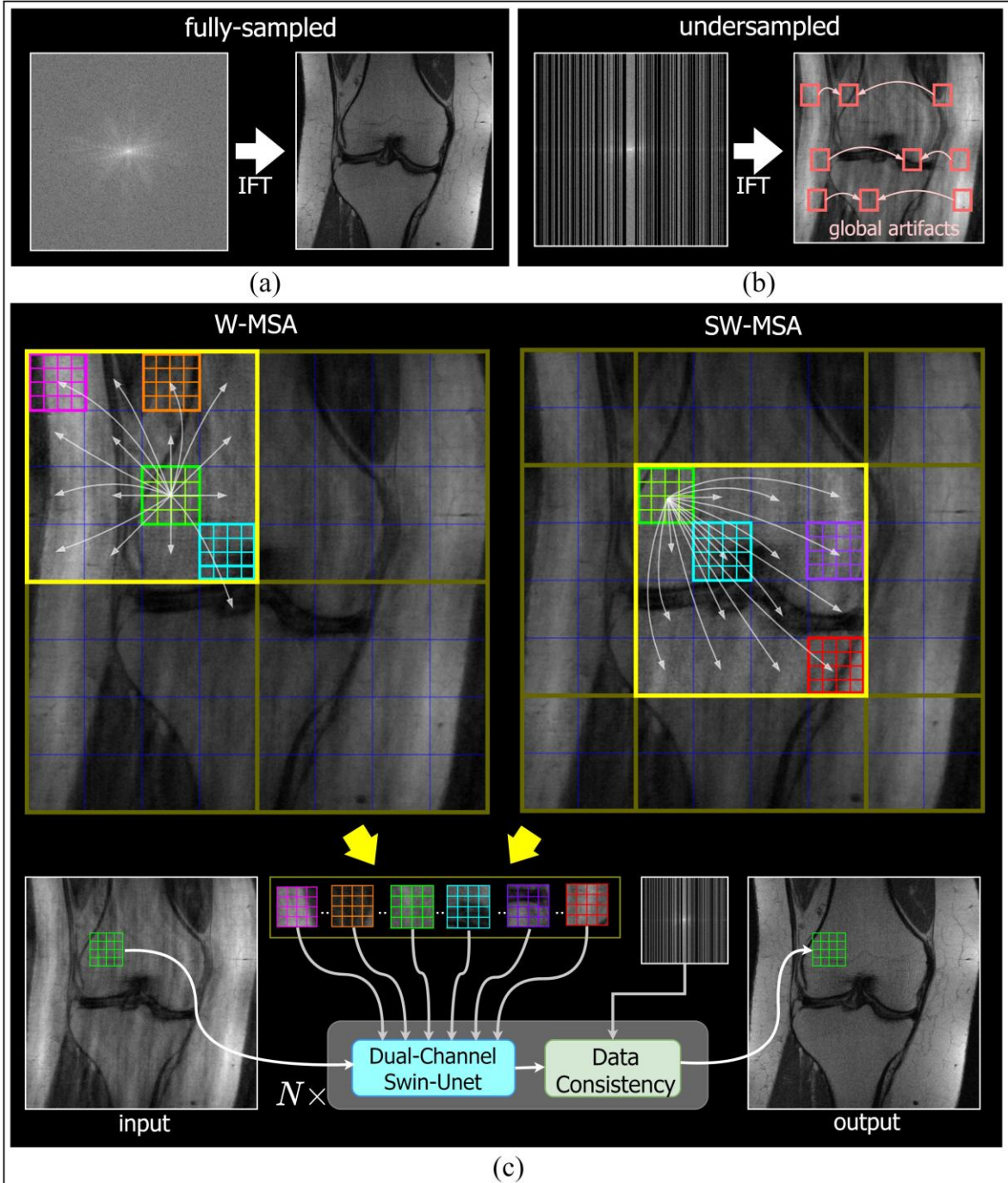


Fig. 1. (a) Fourier reconstruction from fully sampled k-space data. (b) Fourier reconstruction from undersampled k-space data causing global artifacts. (c) W-MSA and SW-MSA which are administered by two consecutive transformers within the Swin transformer used in McSTRA. The figure depicts how an image patch (light green) is able to broaden its receptive field and capture global features via the shifted window mechanism and self-attention.

3.2 Deep Learning Formulation

In order to reconstruct \mathbf{x} from $\hat{\mathbf{y}}$, the following regularized optimization can be used (Schlemper et al., 2018):

$$\mathbf{x}^* = \underset{\mathbf{x}}{\operatorname{argmin}} \{ \mathcal{R}(\mathbf{x}) + \lambda \|\hat{\mathbf{y}} - \mathbf{M} \odot (\mathbf{F}\mathbf{x})\|_2^2 \} \quad (1)$$

where the $\mathcal{R}(\cdot)$ performs regularization, e.g. based on sparsity priors (Lustig et al., 2007; Ravishankar and Bresler, 2011) or network priors (Wang et al., 2016). The second term ensures data fidelity and $\lambda \in \mathbb{R}$ allows the balance of data fidelity based on the acquisition noise level (Schlemper et al., 2018). Most of the DL-based reconstruction methods are data-driven and end-to-end trainable, therefore, learn a complex high-dimensional regularization function through training data itself. The formulation of the DL-based reconstruction can be presented as follows:

$$\mathbf{x}^* = \underset{\mathbf{x}}{\operatorname{argmin}} \{ \|\mathbf{x} - f_{\text{DL}}(\hat{\mathbf{x}}|\theta)\|_2^2 + \lambda \|\hat{\mathbf{y}} - \mathbf{M} \odot (\mathbf{F}\mathbf{x})\|_2^2 \} \quad (2)$$

where f_{DL} is the forward DL model parameterized by θ which takes an image with artifacts, $\hat{\mathbf{x}}$, as input and produces a reconstruction as output. Given a large set of training data, the DL model can be trained using a predefined loss function such as ℓ_1 -norm (Zbontar et al., 2019), ℓ_2 -norm (Schlemper et al., 2018), categorical cross-entropy (Pawar et al., 2019), or structural similarity (SSIM) index (Zbontar et al., 2019) -based loss functions.

A closed-form solution to the optimization problem in Eq. (2) can be presented as follows:

$$\mathbf{y}_{\text{rec}}(j) = \begin{cases} \mathbf{y}_c(j) & \text{if } j \notin \Omega \\ \frac{\mathbf{y}_c(j) + \lambda \hat{\mathbf{y}}(j)}{1 + \lambda} & \text{if } j \in \Omega \end{cases} \quad (3)$$

where $\mathbf{y}_c = \mathbf{F}\mathbf{x}_c = \mathbf{F}f_{\text{DL}}(\hat{\mathbf{x}}|\theta^*)$ is the k-space of the reconstructed image, \mathbf{x}_c . Parameters, θ^* are the optimized model parameters. Ω indicates the subset of indices sampled from the k-space. The final reconstructed image is given as $\mathbf{x}_{\text{rec}} = \mathbf{F}^H \mathbf{y}_{\text{rec}}$.

3.3 Cascaded Network

As discussed in Section 2, cascaded networks for MRI reconstruction consist of cascaded DL blocks and DC blocks that perform the k-space correction. The forward pass of the DC block can be expressed in matrix form as follows:

$$f_{\text{DC}}(\mathbf{x}_c, \mathbf{y}; \lambda) = \mathbf{F}^H \mathbf{\Lambda} \mathbf{F} \mathbf{x}_c + \frac{\lambda}{1 + \lambda} \mathbf{F}^H (\mathbf{M} \odot \mathbf{y}) \quad (4)$$

where $\mathbf{\Lambda} = \begin{cases} 1 & \text{if } k \notin \Omega \\ \frac{1}{1 + \lambda} & \text{if } k \in \Omega \end{cases}$ is a diagonal matrix. The underlying principle of this cascaded model is that the output of one CNN block is connected to the next CNN block through a DC block, thereby providing a framework which iterates between intermediate de-aliasing and k-space correction. The

first-order derivative of the forward pass in Eq. (4) with respect to the input can be easily expressed as $\frac{\partial f_{DC}}{\partial x_c} = \mathbf{F}^H \boldsymbol{\Lambda} \mathbf{F}$, which enables the whole model to be trained in an end-to-end manner.

3.4 Vision Transformer, Swin Transformer, and Swin-Unet

The basic constituent of transformer networks is the self-attention mechanism. Given a sequence of vectorized image patch tokens $\mathbf{z}_1, \mathbf{z}_2, \dots, \mathbf{z}_n$ by $\mathbf{Z} \in R^{n \times d}$, where d is the dimension of the features, the main aim of self-attention is to capture relationships between all n patches. This is done using three learnable weight matrices named Queries ($\mathbf{W}^Q \in R^{d \times d_q}$), Keys ($\mathbf{W}^K \in R^{d \times d_k}$), and Values ($\mathbf{W}^V \in R^{d \times d_v}$). The output $\mathbf{Z}_{out} \in R^{n \times d_v}$ of a self-attention layer is given by:

$$\mathbf{Z}_{out} = \text{softmax} \left(\frac{\mathbf{Q} \mathbf{K}^T}{\sqrt{d_q}} \right) \mathbf{V} \quad (5)$$

where $\mathbf{Q} = \mathbf{Z} \mathbf{W}^Q$, $\mathbf{K} = \mathbf{Z} \mathbf{W}^K$, and $\mathbf{V} = \mathbf{Z} \mathbf{W}^V$.

Swin transformer, as discussed in Section 2, is a transformer variant which not only operates on local image patches but also models global correlations via a shifted window mechanism (See Fig. 1(c)). For a given sequence of vectorized image patch tokens $\mathbf{z}_1, \mathbf{z}_2, \dots, \mathbf{z}_n$, The operations within the Swin transformer block (See Fig. 3(a)) could be expressed as follows:

$$\hat{\mathbf{z}}^l = \text{W-MSA} \left(\text{LN}(\mathbf{z}^{l-1}) \right) + \mathbf{z}^{l-1} \quad (6)$$

$$\mathbf{z}^l = \text{MLP} \left(\text{LN}(\hat{\mathbf{z}}^l) \right) + \hat{\mathbf{z}}^l \quad (7)$$

$$\hat{\mathbf{z}}^{l+1} = \text{SW-MSA} \left(\text{LN}(\mathbf{z}^l) \right) + \mathbf{z}^l \quad (8)$$

$$\mathbf{z}^{l+1} = \text{MLP} \left(\text{LN}(\hat{\mathbf{z}}^{l+1}) \right) + \hat{\mathbf{z}}^{l+1} \quad (9)$$

where W-MSA and SW-MSA are window and shifted window multi-head self-attention, respectively. $\hat{\mathbf{z}}^l$ and \mathbf{z}^l represents the output tokens of the W-MSA module and its preceding multi-layer perceptron (MLP) module, respectively. $\hat{\mathbf{z}}^{l+1}$ and \mathbf{z}^{l+1} represent the output tokens of the SW-MSA module and its preceding MLP module, respectively. As discussed in Section 2, Swin-Unet, is an Unet-like pure transformer network which contains several Swin transformer blocks as can be seen in Fig. 3(c).

3.5 Point Spread Function

The point spread function fundamentally describes the response to a point object and thus determines the quality of an imaging system as well as the captured image itself. Generally, for a linear, shift-invariant imaging system, the PSF governs the image of any known object via convolution as below (Robson et al., 1997):

$$\mathbf{I} = \mathbf{I}_0 * \mathbf{H} \quad (10)$$

where \mathbf{I} is the underlying object, \mathbf{H} is the PSF of the imaging device, \mathbf{I}_0 is the image captured from the said device, and $*$ is the convolution operation. In MR imaging, the k-space is sampled discretely via analog-to-digital converters utilizing square pulses, hence usually having a PSF of a *sinc* function.

In accelerated MRI, the undersampled image, \mathbf{I}_{und} can be modelled using the PSF corresponding to the undersampling mask, \mathbf{H}_{samp} with respect to the fully sampled reference image, \mathbf{I}_{ref} as below (Tan and Zheng, 2005):

$$\mathbf{I}_{\text{und}} = \mathbf{I}_{\text{ref}} * \mathbf{H}_{\text{samp}} \quad (11)$$

where $\mathbf{H}_{\text{samp}} = \mathbf{F}\mathbf{M}$ which is the Fourier transform of the sampling mask. Thus, the spatial spread of aliasing artifacts directly depends on \mathbf{H}_{samp} , thereby on \mathbf{M} . For instance, 1D undersampling in k-space will spread the aliasing artefacts row-wise in the subsequent aliased image as shown in Fig. 2.

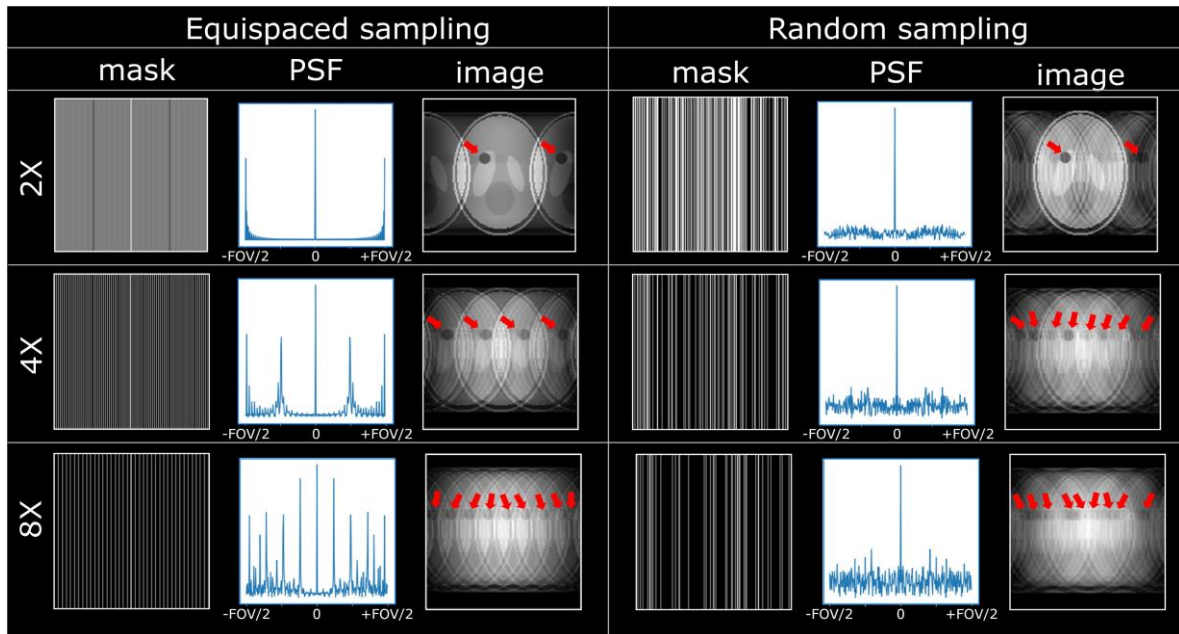


Fig. 2. Different sampling masks, their corresponding PSFs, and the resulting undersampled MR images with artifacts demonstrated on the Shepp–Logan phantom. Note the added dark grey spot which clearly depicts the coherence between the peaks of the PSF and the aliasing artifact pattern in the phantom image.

4 Methods

The overall schematic of the proposed McSTRA model is shown in Fig. 3. It consists of four main architectural components: the multi-head feature extractor which captures image features corresponding to different spectral regions in k-space; the cascaded dual-channel Swin-Unet (DS) blocks interleaved with DC blocks and a discounted intermediate loss computation strategy; the reconstruction tail which enforces magnitude image reconstruction using a single-channel Swin-Unet (SS); the PSF-based, instant-dependent, shared positional embedding generator which incorporates spatial spread in aliasing artifacts pattern. In this Section, we discuss each architectural component of McSTRA separately.

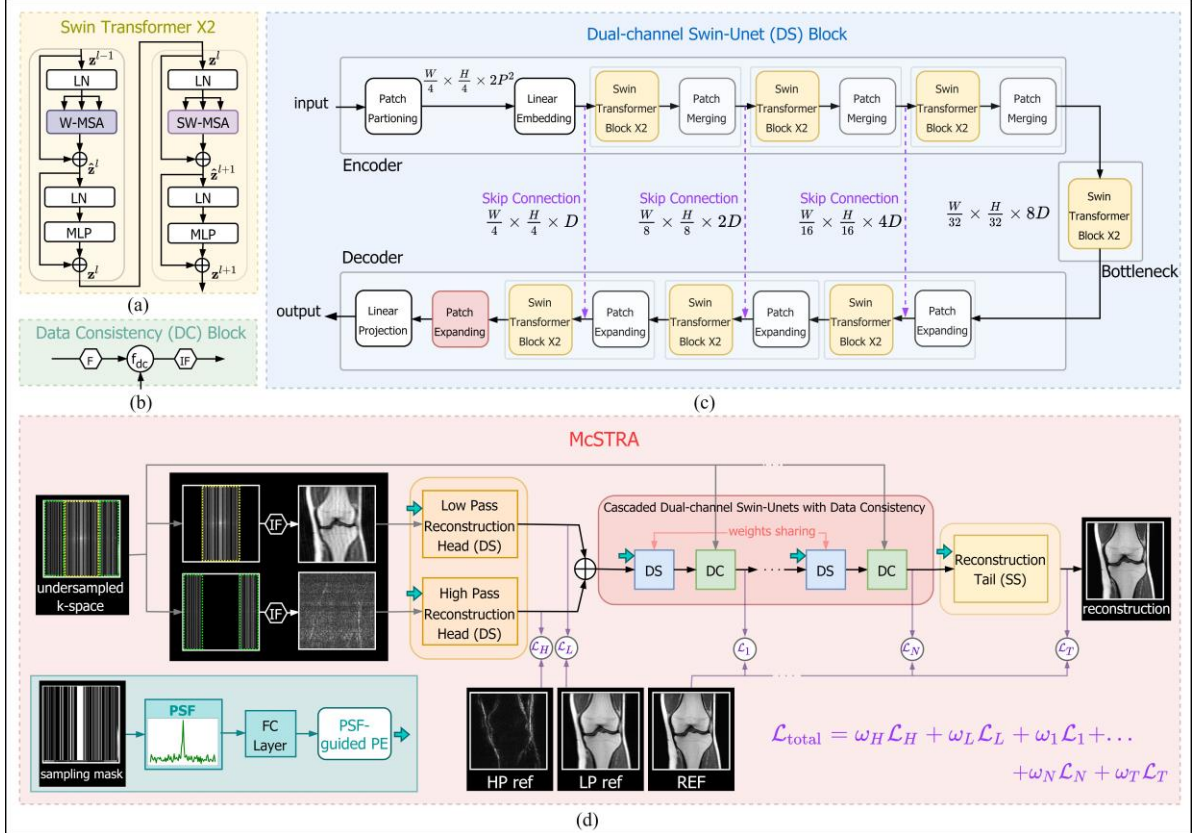


Fig. 3. Overview of McSTRA. (a) Swin transformer X2 block: W-MSA and SW-MSA (b) DC block (c) Swin-Unet architecture (d) Overall McSTRA model

4.1 Multi-head Feature Extractor

Our proposed multi-head feature extractor exploits the spectral properties in k-space by partitioning the k-space and extracting meaningful features separately. The multi-head setup contains two heads. The low-pass head is fed with only the low-frequency image features whereas the high-pass head is fed with only the high-frequency image features as seen in Fig. 3(d). The intention here is to dedicate two distinguished sets of model parameters to learn the reconstruction of high- and low-frequency information of the image separately so that the high-frequency MR features will receive sufficient attention within the model. In the end, the outputs of the two heads will be fused together and passed down to the cascaded DS. As high- and low-pass heads, we utilize dual-channel Swin-

Unet (DS) blocks which are fundamentally equivalent to the Swin-Unet (Cao et al., 2021), but designed to handle complex MR data using two-channel input/output formation.

Given the undersampled k-space $\hat{\mathbf{y}}$ as input, the output from the multi-head setup, \mathbf{x}_{head} can be expressed as below:

$$\mathbf{x}_l = f_l(\mathbf{F}^H(\mathbf{M}_l \odot \hat{\mathbf{y}}) | \theta_l) \quad (12)$$

$$\mathbf{x}_h = f_h(\mathbf{F}^H(\mathbf{M}_h \odot \hat{\mathbf{y}}) | \theta_h) \quad (13)$$

$$\mathbf{x}_{\text{head}} = \mathbf{x}_l + \mathbf{x}_h \quad (14)$$

where \mathbf{x}_l and \mathbf{x}_h are the outputs from the low- and high-pass heads, respectively. f_l and f_h represent the DS blocks corresponding to low-pass and high-pass heads, respectively. \mathbf{M}_l and \mathbf{M}_h are sampling masks which extract the center and outer regions of the undersampled k-space, respectively. In order to enforce additional regularization in terms of feature extraction, we compute the loss of individual heads and sum them up to contribute to the total loss of the model as below:

$$\mathcal{L}_{\text{head}} = \alpha_l \cdot \mathcal{L}(\tilde{\mathbf{x}}_l, \mathbf{x}_l) + \alpha_h \cdot \mathcal{L}(\tilde{\mathbf{x}}_h, \mathbf{x}_h) \quad (15)$$

where $\tilde{\mathbf{x}}_l = \mathbf{F}^H(\mathbf{M}_l \odot \mathbf{y})$ and $\tilde{\mathbf{x}}_h = \mathbf{F}^H(\mathbf{M}_h \odot \mathbf{y})$ are the reference images corresponding to the low- and high-pass heads, respectively. We chose $\alpha_l = \alpha_h = \frac{1}{2}$.

4.2 Cascaded Dual-channel Swin-Unets

The cascaded DS blocks as seen in Fig. 3(d) are interleaved with DC blocks which perform correction in k-space as discussed in Section 2. McSTRA consists of N number of DS blocks interleaved with DC blocks forming an iterative cascade. Given the forward function of the t^{th} DS block of the cascade as f_{cas} with parameters $\{\theta_{cas}^t\}_{t=1}^N$, the undersampled k-space, $\hat{\mathbf{y}}$ and the output from the multi-head setup, \mathbf{x}_{head} , the output after the t^{th} iteration can be expressed (following Eq. 4) as follows:

$$\mathbf{x}_t = \mathbf{F}^H \mathbf{A} \mathbf{F} f_{cas}(\mathbf{x}_{t-1} | \theta_{cas}^t) + \frac{1}{1 + \lambda} \mathbf{F}^H \hat{\mathbf{y}}, \quad t = 1, 2, \dots, N \quad (16)$$

where $\mathbf{x}_0 = \mathbf{x}_{\text{head}}$. Note that in our proposed framework, we share weights among the DS blocks for efficient computational memory usage, thus $\theta_{cas}^1 = \theta_{cas}^2 = \dots = \theta_{cas}^N$. We compute a discounted loss along the cascade as below:

$$\mathcal{L}_{\text{cas}} = \sum_{t=1}^N \beta_t \cdot \mathcal{L}(\tilde{\mathbf{x}}, \mathbf{x}_t) \quad (17)$$

where $\tilde{\mathbf{x}} = \mathbf{F}^H \mathbf{y}$ is the reference image. As seen in Eq. (17), not only the final reconstruction of the cascade, \mathbf{x}_N , but also the intermediate reconstructions, \mathbf{x}_t , contribute to \mathcal{L}_{cas} multiplied by a discounted scale factor β_t . We set β_t to increase linearly with t , i.e., $\beta_t = t / \sum_{k=1}^N k$ which enforces McSTRA to learn accurate MRI reconstructions incrementally. These intermediate loss computations also help to combat the vanishing gradients by additional regularization (Szegedy et al., 2015).

4.3 Reconstruction Tail

In McSTRA, the reconstruction heads, as well as the cascaded DS, perform mappings from two-channel inputs to two-channel outputs facilitating real and imaginary parts of complex MR data. We design the reconstruction tail to construct the final magnitude image which is often utilized for clinical applications. As the reconstruction tail architecture, we use a single-channel Swin-Unet (SS) to perform a magnitude image to magnitude image mapping. It is noted that the reconstruction tail can also be extended for the reconstruction of complex images. The forward function of the reconstruction tail can be expressed as below:

$$\mathbf{x}_{\text{tail}} = f_{\text{tail}}(\mathbf{x}_{\text{cas}} | \theta_{\text{tail}}) \quad (18)$$

Note that \mathbf{x}_{cas} in Eq. (18) represents the magnitude image of the output from the cascaded DS. The tail loss is computed between \mathbf{x}_{tail} and the magnitude reference image, $\tilde{\mathbf{x}}$ as $\mathcal{L}_{\text{tail}} = \mathcal{L}(\tilde{\mathbf{x}}, \mathbf{x}_{\text{tail}})$.

4.4 Loss Function

For a given batch during training, the total loss of McSTRA would be the weighted average of $\mathcal{L}_{\text{head}}$, \mathcal{L}_{cas} , and $\mathcal{L}_{\text{tail}}$ computed as below:

$$\mathcal{L}_{\text{total}}(\theta) = \gamma_{\text{head}} \cdot \mathcal{L}_{\text{head}} + \gamma_{\text{cas}} \cdot \mathcal{L}_{\text{cas}} + \gamma_{\text{tail}} \cdot \mathcal{L}_{\text{tail}} \quad (19)$$

where θ represents all the trainable parameters of McSTRA. In our implementation, we chose $\gamma_{\text{head}} = \gamma_{\text{cas}} = \gamma_{\text{tail}} = \frac{1}{3}$. Based on $\mathcal{L}_{\text{total}}$, back-propagation will be performed to update all the trainable parameters of the model including the positional embedding generation network discussed in Section 4.5.

4.5 Point Spread Function-based Positional Embedding Generator

As discussed in Section 2, positional embeddings play a vital role in transformer networks in order to leverage the order of the sequence of tokens. As discussed in Section 3.5, the spatial spread of aliasing artifacts directly depends on the PSF. Thus, to guide the self-attention operations within the transformer layers, we proposed a semi-network which takes the PSF corresponding to the input image and generates a positional embedding for the respective input. This type of positional embedding could especially be beneficial in a random undersampling setting where each input is subjected to a unique undersampling pattern, hence consisting of a unique aliasing pattern compared with the rest of the inputs in the training dataset. Given the PSF-based positional embedding generator network as \mathcal{P} , and the sampling mask for a given input as \mathbf{M} , the total positional embedding for a given input is computed as below:

$$\mathbf{E}_{\text{pos}} = \mathcal{P}(\mathbf{H}_{\text{samp}} | \theta_{\mathcal{P}}) + \mathbf{E}_{\text{abs}} \quad (20)$$

where \mathbf{E}_{abs} is the conventional 1D positional embedding as in (Dosovitskiy et al., 2021). As \mathcal{P} , we utilize a fully connected layer so that the resulting positional embedding for each pixel could be interpreted as weighted average of the underlying PSF. The parameters, $\theta_{\mathcal{P}}$ are updated using

backpropagation on the total loss computation in Eq. (19). Moreover, we share the positional embedding, E_{pos} across all Swin-Unets in McSTRA.

4.6 Implementation

For the self-attention layers in the multi-head setup, the cascaded DS, and the reconstruction tail, we utilize an embedding dimension of 48, 96, and 48 respectively. As the loss, \mathcal{L} , for all computations we utilized ℓ_1 -norm-based loss (Zbontar et al., 2019). We implement five iterations within the cascade, i.e., $N = 5$ following similar formulation as in (Schlemper et al., 2018). McSTRA was trained on an NVIDIA A40 GPU for 50 epochs in a batch size of 8 using RMSProp optimizer with a learning rate of $1e^{-4}$.

5 Experiments And Results

In this Section, we present the empirical results of the experiments that we conducted in order to assess the validity of McSTRA as a compatible solution for accelerated MRI Reconstruction.

5.1 Experimental Setting

Datasets and Preprocessing. For the training and validation of the McSTRA, the fastMRI knee and brain datasets (<https://fastmri.org/dataset/>) were utilized. The knee dataset consists of fully sampled knee MR k-space data obtained on 1.5 and 3.0 Tesla magnets. The raw complex k-space data include coronal proton density-weighted data with and without fat suppression (PDFS and PD respectively). The exact number of MR volumes and 2D slices utilized for training and validation are given in Table I. All models (McSTRA and other comparative methods) were trained on PD and PDFS data together. The intensity values of the knee data were scaled in the range [0,1] to avoid vanishing gradients which could cause training to fail.

Table I. The numbers of volumes and 2D slices of the fastMRI knee dataset.

Sequence	Training	Validation	Total
PD	484 [17286]	100 [3592]	584 [20878]
PDFS	489 [17456]	99 [3543]	588 [20999]
Total	973 [34742]	199 [7135]	1172 [41877]

Undersampling. The input to the model is undersampled complex k-space data which were obtained by retrospectively masking k-space lines in the phase encoding direction. Following a similar undersampling procedure to Zbontar et al. (2019), during training, we applied the same undersampling mask to all the slices in a given volume with a random four-fold acceleration while retaining 8% of the center frequencies.

Comparative Methods. In order to assess the competitiveness of the proposed model, we compared its reconstruction accuracy with several other state-of-the-art DL-based MRI reconstruction

methods, i.e. the fastMRI U-Net baseline (Zbontar et al., 2019), a deep cascade of CNNs (D5C5) (Schlemper et al., 2018), MRI dual-domain reconstruction network (MD-Recon-Net) (Ran et al., 2021), and the vision transformer (ViT) (Dosovitskiy et al., 2021). For the fairness of comparison, we sustained the original hyperparameters and the training details for these models following their original literature.

Evaluation Metrics. For quantitative performance evaluation purposes, we utilize three commonly used metrics, i.e., normalized mean square error (NMSE), peak signal-to-noise ratio (PSNR), and structural similarity (SSIM) following formal definitions in Zbontar et al. (2019). We present the volume-wise mean as well as standard error (e.g., Figures 4, 6, 8, 10, and Tables II, III, IV) with respect to the above metrics in order to better comprehend the confidence level of quantitative scores.

5.2 Reconstruction Performance

Fig. 4 summarizes the quantitative reconstruction performance of different methods on the fastMRI knee validation dataset where we present the results for PD and PDFS data separately and together (Overall). Here the undersampling utilized is the same as the training setting, i.e., random four-fold acceleration while retaining 8% of the center frequencies. It can be seen that McSTRA outperforms all the other comparative methods in terms of NMSE, PSNR, and SSIM. It was also observed that generally, PDFS reconstructions show inferior performance than PD reconstructions mainly due to the inherent noise in PD acquisitions of the fastMRI dataset. Fig. 5 shows an example PD knee slice reconstruction from the fastMRI validation dataset. It demonstrates the superiority of McSTRA in reconstructing fine anatomical details unlike the other CNN-based methods such as U-Net and MD-Recon-Net which produce blurry outputs where fine anatomical details are present. It also demonstrates McSTRA’s superior capability in reconstructing anatomical boundary features (see the red and yellow patches in Fig. 5) and textural details in bone (see the blue patch in Fig. 5) which specifically is a consequence of the multi-head setup which enforces sufficient attention within the overall network to the high-frequency MR features which often contains resolution and edge information.

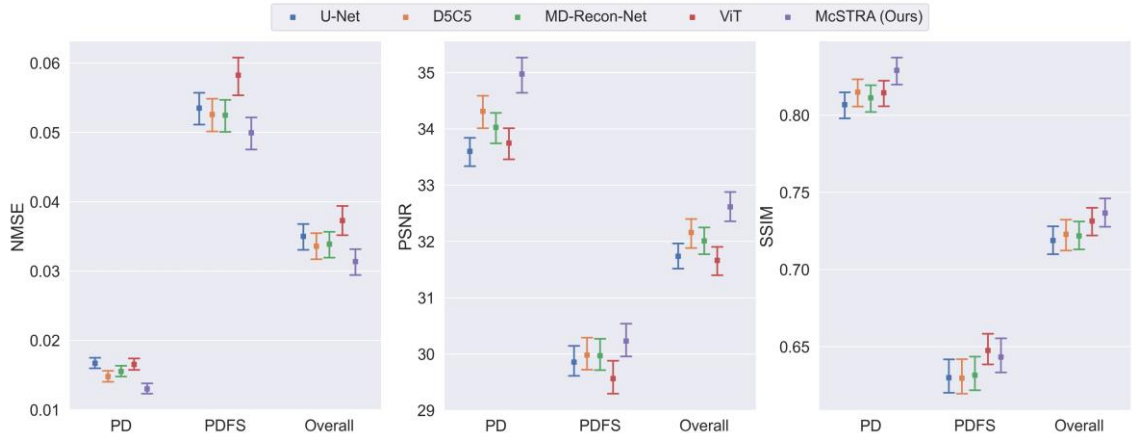


Fig. 4. Quantitative performance comparison of McSTRA under random four-fold acceleration while retaining 8% of the center frequencies on the fastMRI knee validation dataset.

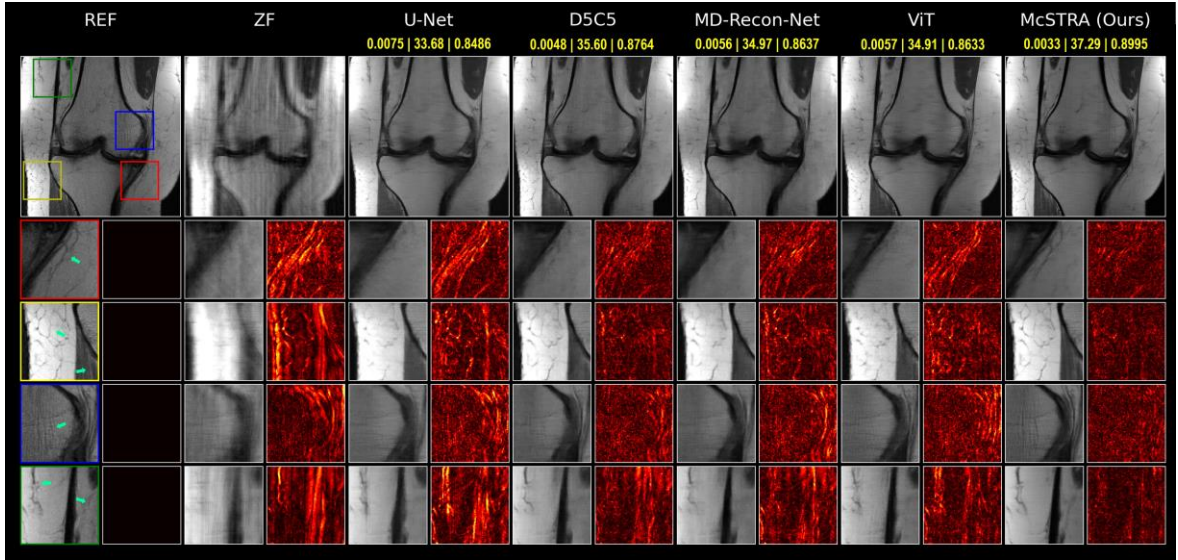


Fig. 5. A PD knee slice reconstruction from the fastMRI validation dataset using different methods under four-fold acceleration while retaining 8% of the center frequencies (Row 1). The NMSE, PSNR, and SSIM scores for each method for the reconstructed slice are displayed on the top (in yellow). Four regions of interest (red, yellow, blue, and green patches) and their corresponding error images are enlarged side-by-side in Rows 2-5. We direct readers' attention to the green arrows shown in the reference image which indicate fine anatomical features.

5.3 Robustness to Noise

In this experiment, we evaluated the robustness of McSTRA to noisy MR acquisitions. We introduced complex additive Gaussian noise to the input k-space measurements (baseline), thereby, simulating signal-to-noise ratio (SNR) levels of 50, 20, 15, 10, 5, and 0 dB, and observed the reconstruction performance of McSTRA and other comparative methods on the fastMRI knee validation dataset. Here the undersampling utilized is the same as the training setting. We present the results for PD and PDFS data together in Fig. 6 which depicts the quantitative reconstruction performance of different methods at different SNR levels. It can be seen that McSTRA outperforms all methods at all noise levels. Note that the results for U-Net and ViT at 0 dB are not shown due to the large deterioration of those methods at 0 dB. It is also seen that the performance gap between McSTRA and other methods with respect to NMSE, PSNR, and SSIM increases with SNR which is an indication of how comparatively well McSTRA oversees noisy data. This point is further verified in Fig. 7 where we visualize reconstructions of a PD knee slice from the fastMRI validation dataset under different SNR levels. Generally, for SNR levels above 15 dB, all methods are able to reconstruct most of the fine features in bone and tissue. But, for SNR levels below 15 dB, it can be seen that CNN-based methods such as D5C5 and Md-Recon-Net drastically fail to reconstruct fine features. It is also worthwhile to note, that even when the SNR is 0 dB where noise power is equal to signal power, McSTRA is still able to reconstruct images with reasonable contrast whereas MD-Recon-Net and ViT demonstrate significant errors.

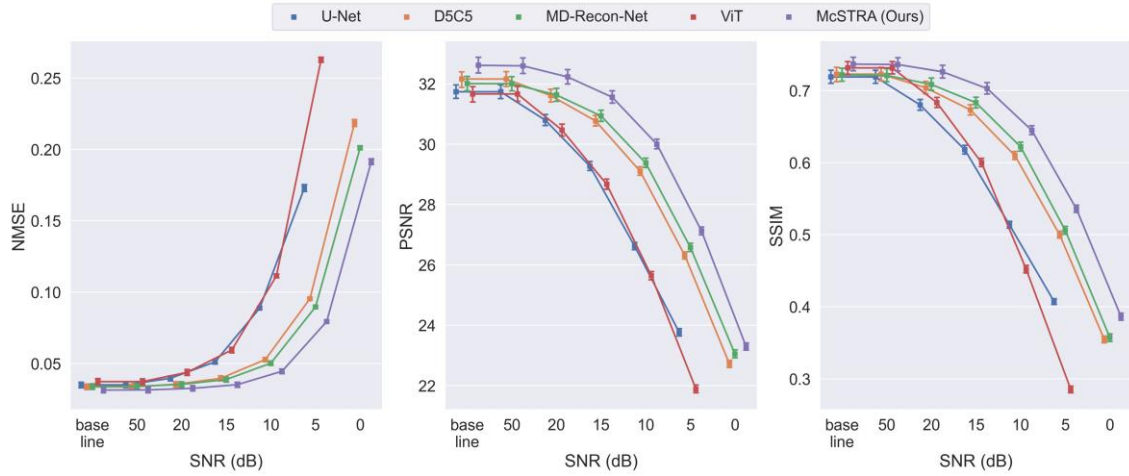


Fig. 6. Quantitative reconstruction performance of McSTRA at different SNRs under random four-fold acceleration while retaining 8% of the center frequencies on the fastMRI knee validation dataset (PD and PDFS together).

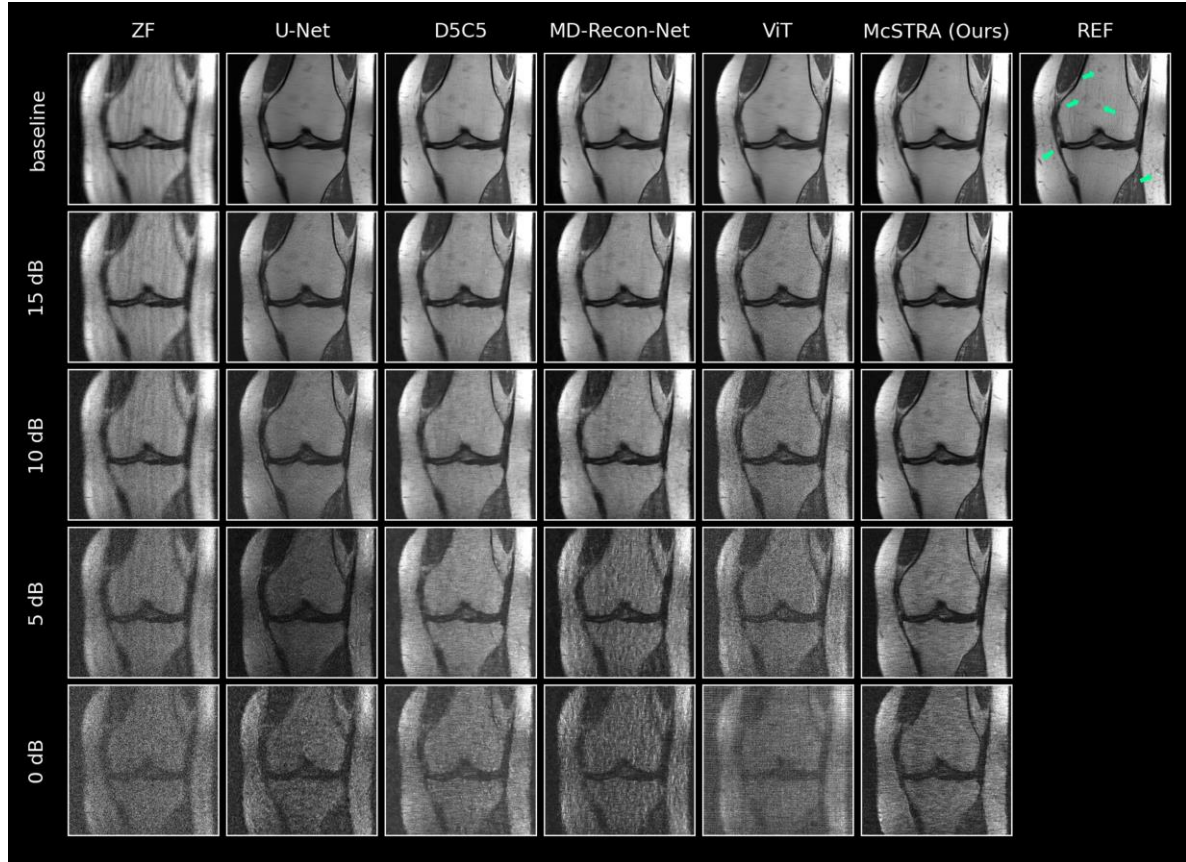


Fig. 7. A PD knee slice reconstruction from the fastMRI validation dataset under different SNR levels. We direct readers' attention to the green arrows in the reference image which indicate fine anatomical features.

5.4 Sampling Changes during Inference

In this experiment, we studied the robustness of McSTRA to different sampling settings with respect to acceleration factor and mask type.

5.4.1 Changes in Acceleration Factor

Here we increased the acceleration factor from 4 to 12 in steps of two and assessed the reconstruction performance of McSTRA and other comparative methods on the fastMRI knee validation dataset. We present the results for PD and PDFS data together in Fig. 8. McSTRA’s performance in terms of NMSE, PSNR, and SSIM drops with accelerations factor in a linear manner, however, it outperforms all other methods with respect to NMSE and PSNR under all acceleration factors. In terms of SSIM, McSTRA’s performance is lower only than ViT at acceleration factors of 8, 10, and 12.

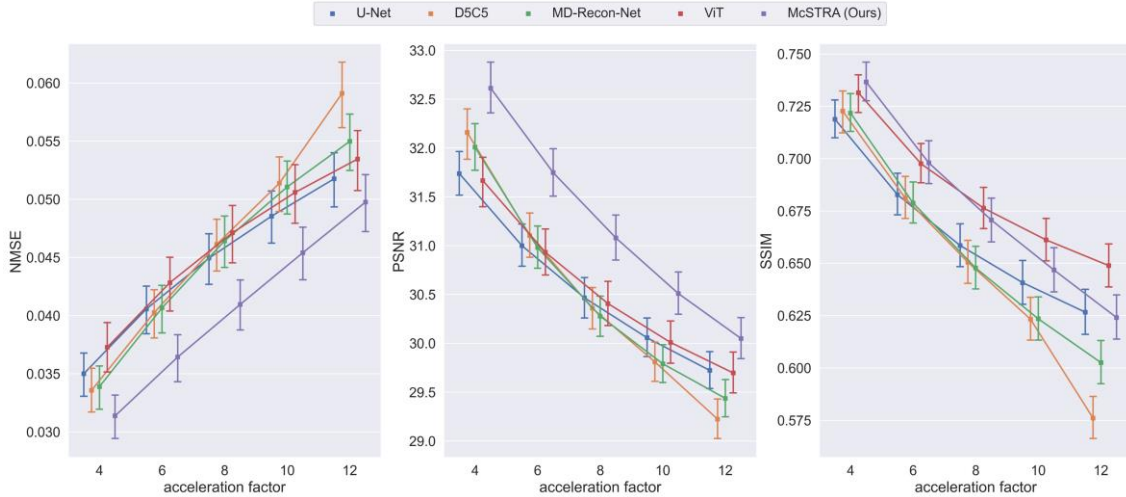


Fig. 8. Quantitative performance inference of McSTRA at different acceleration factors while retaining 8% of the center frequencies on the fastMRI knee validation dataset (PD and PDFS together).

5.4.2 Changes in Mask Type

In this experiment, we assessed the reconstruction performance of McSTRA with equispaced k-space sampling on the fastMRI knee validation dataset. We present the results for PD and PDFS data together in Table II which demonstrates that McSTRA is able to retain superior performance in terms of NMSE, PSNR, and SSIM. Note that the change in performance of McSTRA is minute when compared to the results of the random sampling scenario in Section 5.2 (Fig. 4) which is an indication of the robustness of McSTRA to the undersampling protocol.

Table II. Quantitative performance inference of McSTRA for equispaced sampling protocol in k-space under four-fold acceleration while retaining 8% of the center frequencies on the fastMRI knee validation dataset (PD and PDFS together) (best performance in boldface).

Method	NMSE \downarrow	PSNR \uparrow	SSIM \uparrow
U-Net	0.0351 ± 0.0017	31.69 ± 0.22	0.7178 ± 0.0092
D5C5	0.0336 ± 0.0018	32.12 ± 0.25	0.7221 ± 0.0096
MD-Recon-Net	0.0339 ± 0.0018	31.97 ± 0.24	0.7208 ± 0.0093
ViT	0.0372 ± 0.0020	31.65 ± 0.25	0.7307 ± 0.0087
McSTRA (Ours)	0.0314 ± 0.0018	32.61 ± 0.27	0.7361 ± 0.0096

5.5 Inference on Brain MR Data

In this experiment, we evaluated the performance of McSTRA on brain MR data. We utilized the models that were trained on the fastMRI knee dataset to reconstruct brain slices of the fastMRI brain validation dataset which was also retrospectively undersampled with a random four-fold acceleration while retaining 8% of the center frequencies. The fastMRI brain validation dataset consists of more than 1378 fully sampled knee MR k-space volumes (21842 slices) obtained on 3 and 1.5 Tesla magnets. The raw k-space dataset includes axial T1 weighted, T2 weighted, and FLAIR images. Some of the T1 weighted acquisitions included admissions of a contrast agent (T1POST). We present the results for T1, T1POST, T2, and FLAIR reconstructions separately and together (Overall) in Table III where it can be observed that McSTRA demonstrates superior performance across all image sequences in terms of NMSE, PSNR, and SSIM. Note that, McSTRA achieves remarkably high PSNR and SSIM (e.g., T1POST: PSNR of 38.68 ± 0.11 and SSIM of 0.9536 ± 0.0008) despite the fact that the model was trained on PD and PDFS knee data. Fig. 9 shows an example reconstruction of a T1 brain slice from the fastMRI brain validation dataset which further illustrates that McSTRA is able to resolve most of the aliasing artifacts while preserving comparatively sharp contrast between grey matter and white matter without model re-training. Here, CNN-based methods such as U-Net drastically fail to generalize and oversee aliasing artifacts, hence producing corrupted images with low quality.

Table III. Quantitative performance inference of McSTRA when inferred on fastMRI brain validation dataset under random four-fold acceleration while retaining 8% of the center frequencies (best performance for each sequence in boldface).

Sequence	Method	NMSE↓	PSNR↑	SSIM↑
T1	U-Net	0.0215 ± 0.0007	33.44 ± 0.13	0.8761 ± 0.0022
	D5C5	0.0077 ± 0.0002	37.85 ± 0.17	0.9327 ± 0.0023
	MD-Recon-Net	0.0106 ± 0.0003	36.46 ± 0.15	0.9196 ± 0.0025
	ViT	0.0163 ± 0.0003	34.53 ± 0.14	0.9073 ± 0.0027
	McSTRA (Ours)	0.0066 ± 0.0002	38.54 ± 0.18	0.9410 ± 0.0023
T1POST	U-Net	0.0181 ± 0.0003	33.92 ± 0.08	0.8953 ± 0.0012
	D5C5	0.0074 ± 0.0002	37.90 ± 0.10	0.9444 ± 0.0009
	MD-Recon-Net	0.0099 ± 0.0002	36.56 ± 0.10	0.9334 ± 0.0010
	ViT	0.0147 ± 0.0002	34.78 ± 0.08	0.9202 ± 0.0010
	McSTRA (Ours)	0.0062 ± 0.0001	38.68 ± 0.11	0.9536 ± 0.0008
T2	U-Net	0.0301 ± 0.0003	30.44 ± 0.05	0.8580 ± 0.0007
	D5C5	0.0133 ± 0.0002	34.12 ± 0.07	0.9175 ± 0.0008
	MD-Recon-Net	0.0181 ± 0.0002	32.72 ± 0.07	0.9009 ± 0.0008
	ViT	0.0240 ± 0.0002	31.40 ± 0.06	0.8865 ± 0.0007
	McSTRA (Ours)	0.0109 ± 0.0001	34.95 ± 0.07	0.9312 ± 0.0007
FLAIR	U-Net	0.0253 ± 0.0009	32.83 ± 0.20	0.8275 ± 0.0045
	D5C5	0.0102 ± 0.0003	36.80 ± 0.25	0.8936 ± 0.0049
	MD-Recon-Net	0.0131 ± 0.0004	35.69 ± 0.24	0.8778 ± 0.0053
	ViT	0.0178 ± 0.0006	34.34 ± 0.24	0.8652 ± 0.0049
	McSTRA (Ours)	0.0089 ± 0.0003	37.38 ± 0.27	0.9084 ± 0.0044
Overall	U-Net	0.0262 ± 0.0003	31.72 ± 0.06	0.8656 ± 0.0008
	D5C5	0.0111 ± 0.0001	35.57 ± 0.07	0.9231 ± 0.0008
	MD-Recon-Net	0.0151 ± 0.0002	34.21 ± 0.07	0.9082 ± 0.0009
	ViT	0.0206 ± 0.0002	32.72 ± 0.06	0.8944 ± 0.0008

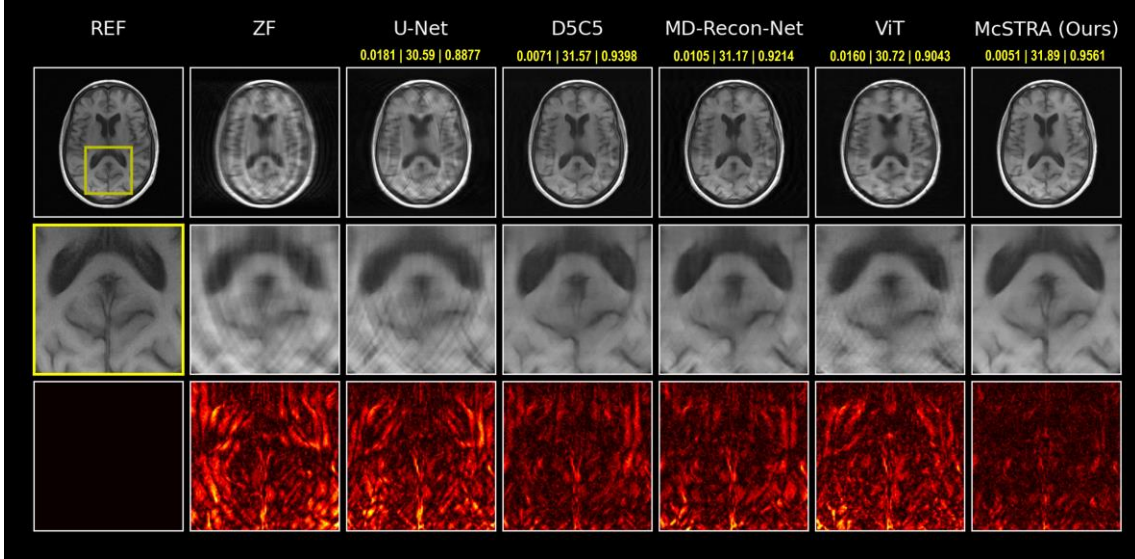


Fig. 9. Inference on a T1 brain slice from the fastMRI brain validation dataset under random four-fold acceleration while retaining 8% of the center frequencies (Row 1). The NMSE, PSNR, and SSIM scores for each method for the reconstructed slice are displayed on the top (in yellow). The regions of interest (yellow patch) and their corresponding error images are enlarged in Rows 2 and 3, respectively.

5.6 Robustness to Abnormalities

Irrespective of the drastic improvement in accelerated MRI using DL, false-negative reconstructions are still a concerning issue (Antun et al., 2020). During the presentation of results of the fastMRI challenge 2019 and 2020 (<https://slideslive.com/38922093/medical-imagingmeets-neurips-4>), it was revealed that even high-performing DL models are unable to reconstruct small abnormalities such as meniscal tear and subchondral osteophytes. Further, the results of the study conducted by Recht et al. (2020) demonstrate that it is often difficult to reconstruct small structures near the knee joint which could be clinically relevant not only for diagnosis but also for the treatment of lesions. In support of battling such adversarial attacks on image reconstruction, Calivá et al. (2021) manually annotated MRI slices of the fastMRI knee dataset which contain lesions.

In this experiment, we evaluated our trained models on those MRI volumes identified by Calivá et al. (2021) from the fastMRI knee validation dataset (which includes both PD and PDFS knee data) in order to determine McSTRA’s ability to battle abnormalities in anatomical structures. Fig. 10 presents quantitative scores categorized based on the location of the knee where the lesion is present, i.e., bone marrow, cartilage, meniscus, or cyst. It is seen that McSTRA is able to achieve high PSNR and SSIM, especially when the lesion exists in the bone marrow or cartilage. The performance is comparatively high even when the lesion exists in the cyst compared to other methods like ViT and CNN-based methods like U-Net which show inferior capabilities for reconstructing abnormalities in terms of NMSE, PSNR, and SSIM.

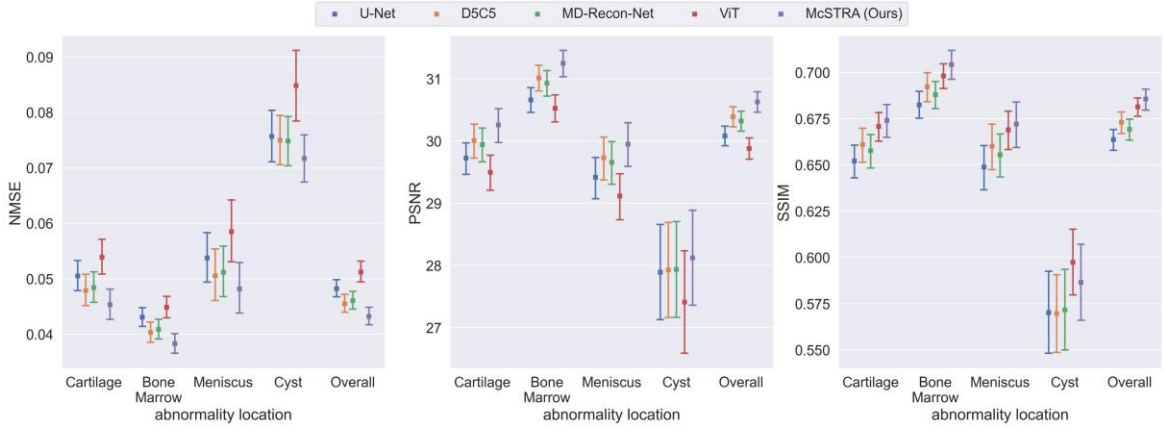


Fig. 10. Quantitative performance comparison of McSTRA under random four-fold acceleration while retaining 8% of the center frequencies on the fastMRI knee validation volumes which were identified to contain lesions by Calivá et al. (2021).

5.7 Ablation Studies

Here, we assessed the effectiveness of each constituent component of McSTRA and their contribution to the overall improved performance of McSTRA.

5.7.1 Effectiveness of the Multi-head Feature Extraction

Here we performed experiments with and without the multi-head setup on the fastMRI knee validation dataset. We present the results for PD and PDFS data together in Table IV where it can be seen that the multi-head feature extraction setup which focuses on complementary k-space regions improves the performance of McSTRA for accurate MRI reconstruction in terms of NMSE, PSNR, and SSIM.

5.7.2 Effectiveness of the Cascaded Network

Here we assessed the effectiveness of the cascaded network of Swin-Unets and the intermediate loss computations. We trained and evaluated McSTRA with and without intermediate loss computations after each iteration. We present the results for PD and PDFS data together on the fastMRI knee validation dataset in Fig. 11 where the performance gradually increases through the cascade for the model with the intermediate loss computations resulting in a better final performance in terms of NMSE, PSNR, and SSIM. Even the model without the intermediate loss computations shows increments in performance through the cascade, but those increments are not gradual resulting in a lower final performance in terms of NMSE, PSNR, and SSIM. Fig. 11 also shows that the difference in the performance of the two models converges with iterations which is an indication that the model trained without intermediate loss computations reconstructs more accurate images during the later iterations and not during the earlier iterations. This signifies that the backpropagation of the overall loss does not propagate to the first several iterations sufficiently.

In contrast, the model with intermediate loss computations at each iteration enforces accurate reconstruction after each iteration which ultimately leads to a better final performance.

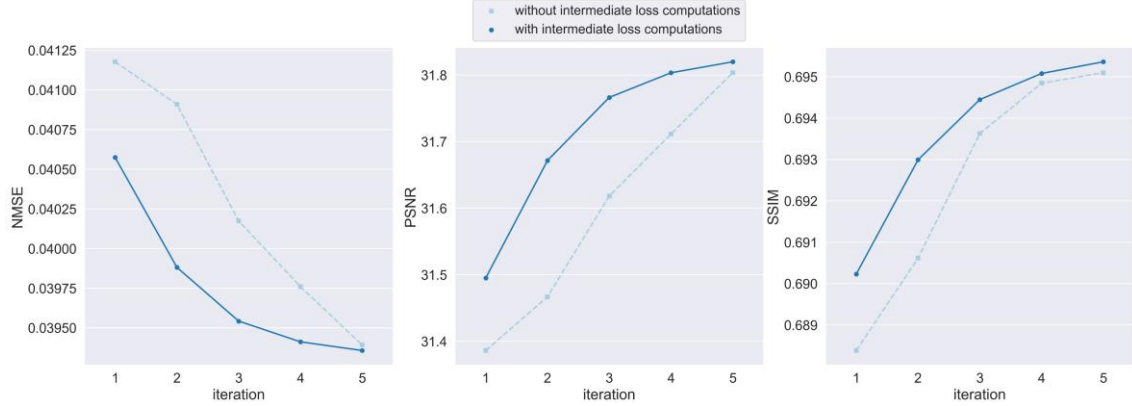


Fig. 11. Comparative reconstruction performance of the models trained with and without the intermediate loss computations under random four-fold acceleration while retaining 8% of the center frequencies on the fastMRI knee validation dataset.

5.7.3 Effectiveness of the PSF guided Positional Embeddings

This experiment shows how PSF guided positional embeddings provide information for McSTRA during the learning process. In Fig. 12, we illustrate the cosine similarity correspondence amongst the PSF guided positional embedding patches. It can be observed that the positional embeddings generated following Eq. (20) learn positional information quite accurately. We illustrate several cosine similarity maps corresponding to different regions of an MR slice selected from the fastMRI knee validation dataset. It is observed that these positional embeddings have been able to direct attention to the image patches with similar anatomical information. The effectiveness of the positional embeddings on quantitative image reconstruction performance is shown in Table IV where it is evident that the PSF guided positional embedding generation contributes to the improvement of reconstruction accuracy.

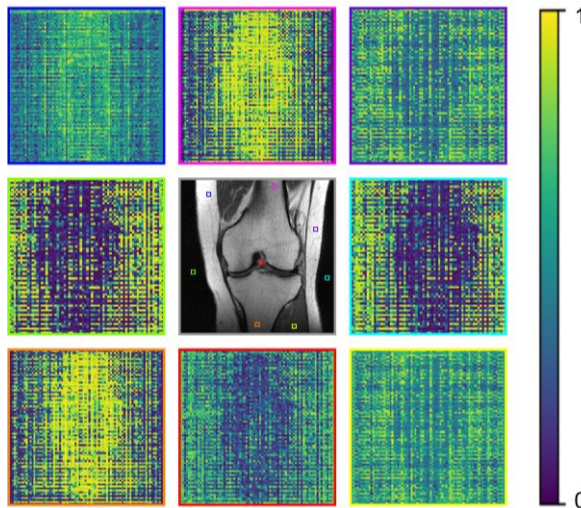


Fig. 12. Cosine similarity between positional embeddings corresponding to some selected patches (demonstrated using distinct colors) of the image and the positional embeddings corresponding to the rest of the patches of the center image.

Table IV. Quantitative reconstruction performance of McSTRA with and without its constituent architectural components under random four-fold acceleration while retaining 8% of the center frequencies on the fastMRI knee validation dataset. Case I: Cascaded of DS and reconstruction tail only, Case II: Cascaded of DS, reconstruction tail, and PSF guided positional embedding generator only, Case III: Multi-head feature extractor, cascaded DS, reconstruction tail, and PSF guided positional embedding generator (McSTRA) (best performance in boldface).

Method	NMSE \downarrow	PSNR \uparrow	SSIM \uparrow
Case I	0.0317 ± 0.0018	32.54 ± 0.27	0.7337 ± 0.0096
Case II	0.0315 ± 0.0018	32.58 ± 0.27	0.7351 ± 0.0096
Case III	0.0314 ± 0.0018	32.61 ± 0.27	0.7366 ± 0.0096

5.8 Convergence Analysis

In Fig. 13, we compare the convergence of the variants of McSTRA presented in previous Sections by providing training and validation curves for the fastMRI knee dataset. It is clearly seen that the final McSTRA has a smoother training loss curve compared to the other variants. Thus, it is evident that the incorporation of the multi-head feature extraction and the PSF-guided positional embedding generation has clearly benefited McSTRA’s convergence.

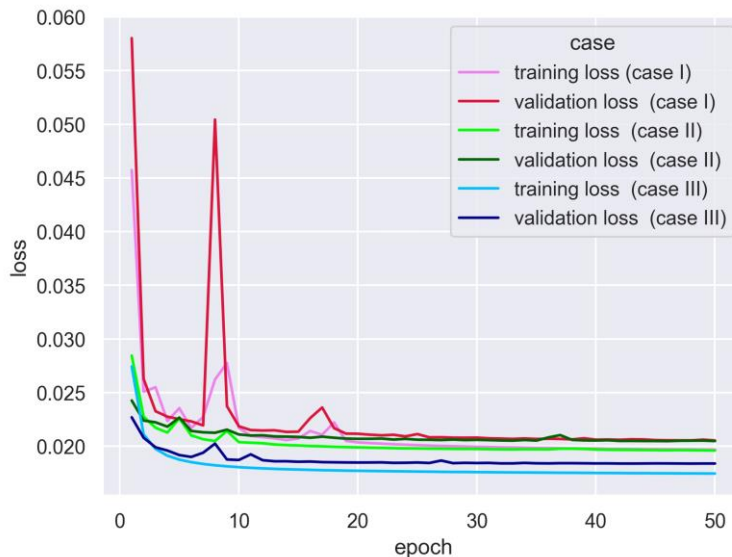


Fig. 13. Training and validation curves of McSTRA and its variants (presented in Table IV) for the fastMRI knee dataset

6 Discussion And Conclusions

In this work, we have introduced a transformer-based DL model which incorporates MR physics for accelerated MRI reconstruction. The overall model is capable of reconstructing high-quality MR images from raw complex MR k-space data outperforming state-of-the-art DL models for MRI reconstruction. In the reported experiments, McSTRA shows superior robustness to adverse conditions such as higher accelerations, noisy data, different undersampling protocols, out-of-distribution data, and abnormalities in anatomy. In the Ablations studies, we illustrate the effect of

each constituent component of McSTRA which confirms the suitability of the underlying rationale behind the conceptual design. McSTRA shows smoother convergence in training compared to its counterpart models without multi-head feature extraction and the PSF-guided positional embedding generation which further illustrates the effectiveness of these architectural components.

One of the key observations from our experiments was the capability of McSTRA to reconstruct fine anatomical features. For instance, the results in Fig. 5 illustrate how edge features in tissue and textural information in bone are recovered during reconstruction by McSTRA whereas the other methods drastically fail to do so. Also, our experiments highlight the capability of McSTRA to oversee noise in k-space measurements. Such improvements are from the global attention mechanism employed in the transformer models. As seen in Fig. 7, even at extreme SNR levels such as 0 dB, McSTRA is able to reconstruct the finest anatomical structures in the knee unlike the CNN-based models such as U-Net and D5C5 which fails to eliminate noise. Furthermore, McSTRA's reconstruction performance with respect to NMSE and PSNR stands out from all other CNN-based models and ViT at exceedingly high accelerations such as 10X and 12X. McSTRA's robustness to sampling protocol is further established by the results in Table II where NMSE, PSNR, and SSIM deteriorates only by a small amount when inferred under an equispaced undersampling setting compared to random undersampling. We believe these outcomes are an indication of the potential of physics-based transformer models to be utilized in the general clinical setting where generalizability and robustness are key requirements.

The inference on the brain dataset further reinforces this rationale where the model that was trained on PD and PDFS knee data displays exceptional de-aliasing capabilities and comparatively high tissue contrast when inferred on T1, T2, and FLAIR brain data. As seen in Fig. 9, CNN-based models such U-Net fails drastically to generalize on different MR sequence and anatomy during inference. McSTRA's ability to oversee out-of-distribution data is further confirmed by the experiments that were conducted on the knee dataset with lesions. The quantitative scores in Fig. 10 clearly demonstrate the superiority of McSTRA in handling abnormalities in the knee which could be extremely beneficial in the clinical setting for diagnosis as well as treatment monitoring.

Despite many strengths, we identify several limitations of the proposed method. One limitation of the proposed model architecture is that it is designed for the single-channel MR acquisition setting whereas many MRI data are acquired in a multi-channel setting. However, this work demonstrates the fundamental principle of McSTRA, and a multi-channel setup can be readily extended based on the current model. In addition, McSTRA has a transformer-based backbone constructed by full-connected layers which do not support varying input sizes. However, this limitation could be overcome by resizing the images before input into the model. In our future work, we would be attempting to overcome these limitations while focusing more on replacing the fully supervised training setting with an unsupervised learning strategy in order to ease the dependency of the reconstruction model on prior data. That way, we would like to make our solutions more robust to out-of-distribution data which is a common concern in medical imaging. Also, we aim to extend our model to be compatible with multi-channel 3D MR data which could be beneficial in terms of exploiting global correlations across the slice dimension and coil sensitivities of the imaging system.

In conclusion, the proposed multi-head, sampling-guided self-attention-based McSTRA model has proven to be successful for the accurate reconstruction of images from undersampled MR data. Both the qualitative and quantitative analysis demonstrated superior performance of McSTRA compared

to state-of-the-art DL reconstruction methods. We believe our contributions would reinforce the establishment of transformer-based DL models for high-quality MRI reconstruction.

Acknowledgments

The authors are grateful for support from Australian Research Council Linkage grant [LP170100494](#) and Australian Research Council Discovery grant [DP210101863](#).

References

- Aggarwal, H.K., Mani, M.P., Jacob, M., 2019. MoDL: Model-Based Deep Learning Architecture for Inverse Problems. *IEEE Trans. Med. Imaging* 38, 394–405.
<https://doi.org/10.1109/TMI.2018.2865356>
- Antun, V., Renna, F., Poon, C., Adcock, B., Hansen, A.C., 2020. On instabilities of deep learning in image reconstruction and the potential costs of AI. *Proc. Natl. Acad. Sci.*
<https://doi.org/10.1073/pnas.1907377117>
- Block, K.T., Uecker, M., Frahm, J., 2007. Undersampled radial MRI with multiple coils. Iterative image reconstruction using a total variation constraint. *Magn. Reson. Med.* 57, 1086–1098.
<https://doi.org/10.1002/mrm.21236>
- Calivá, F., Cheng, K., Shah, R., Pedoia, V., 2021. Adversarial Robust Training of Deep Learning MRI Reconstruction Models. *ArXiv201100070* Cs Eess.
- Cao, H., Wang, Y., Chen, J., Jiang, D., Zhang, X., Tian, Q., Wang, M., 2021. Swin-Unet: Unet-like Pure Transformer for Medical Image Segmentation. *ArXiv210505537* Cs Eess.
- Chaâri, L., Pesquet, J.-C., Benazza-Benyahia, A., Ciuciu, P., 2011. A wavelet-based regularized reconstruction algorithm for SENSE parallel MRI with applications to neuroimaging. *Med. Image Anal.* 15, 185–201. <https://doi.org/10.1016/j.media.2010.08.001>
- Chen, J., Lu, Y., Yu, Q., Luo, X., Adeli, E., Wang, Y., Lu, L., Yuille, A.L., Zhou, Y., 2021. TransUNet: Transformers Make Strong Encoders for Medical Image Segmentation. *ArXiv210204306* Cs.
- Chu, X., Tian, Z., Zhang, B., Wang, X., Wei, X., Xia, H., Shen, C., 2021. Conditional Positional Encodings for Vision Transformers. *ArXiv210210882* Cs.
- Dabov, K., Foi, A., Katkovnik, V., Egiazarian, K., 2006. Image denoising with block-matching and 3D filtering, in: *Image Processing: Algorithms and Systems, Neural Networks, and Machine Learning*. Presented at the *Image Processing: Algorithms and Systems, Neural Networks, and Machine Learning*, SPIE, pp. 354–365. <https://doi.org/10.1117/12.643267>
- Dosovitskiy, A., Beyer, L., Kolesnikov, A., Weissenborn, D., Zhai, X., Unterthiner, T., Dehghani, M., Minderer, M., Heigold, G., Gelly, S., Uszkoreit, J., Houlsby, N., 2021. An Image is Worth 16x16 Words: Transformers for Image Recognition at Scale. *ArXiv201011929* Cs.
- Faris, M., 2021. Segmented Multistage Reconstruction of Magnetic Resonance Images. *Adv. Electr. Comput. Eng.* 21, 107–114. <https://doi.org/10.4316/AECE.2021.04012>
- Faris, M., Javid, T., Rizvi, S.H., Aziz, A., 2021. Segmented Region Based Reconstruction of Magnetic Resonance Image, in: *2021 International Conference on Computer Information Sciences (ICCOINS)*. Presented at the *2021 International Conference on Computer Information Sciences (ICCOINS)*, pp. 68–73. <https://doi.org/10.1109/ICCOINS49721.2021.9497166>
- Feng, C.-M., Yan, Y., Chen, G., Xu, Y., Hu, Y., Shao, L., Fu, H., 2022. Multi-Modal Transformer for Accelerated MR Imaging. *IEEE Trans. Med. Imaging* 1–1.
<https://doi.org/10.1109/TMI.2022.3180228>
- Feng, C.-M., Yan, Y., Fu, H., Chen, L., Xu, Y., 2021. Task Transformer Network for Joint MRI Reconstruction and Super-Resolution, in: de Bruijne, M., Cattin, P.C., Cotin, S., Padoy, N.,

- Speidel, S., Zheng, Y., Essert, C. (Eds.), Medical Image Computing and Computer Assisted Intervention – MICCAI 2021, Lecture Notes in Computer Science. Springer International Publishing, Cham, pp. 307–317. https://doi.org/10.1007/978-3-030-87231-1_30
- Galassi, A., Lippi, M., Torroni, P., 2021. Attention in Natural Language Processing. *IEEE Trans. Neural Netw. Learn. Syst.* 32, 4291–4308. <https://doi.org/10.1109/TNNLS.2020.3019893>
- Griswold, M.A., Jakob, P.M., Heidemann, R.M., Nittka, M., Jellus, V., Wang, J., Kiefer, B., Haase, A., 2002. Generalized autocalibrating partially parallel acquisitions (GRAPPA). *Magn. Reson. Med.* 47, 1202–1210. <https://doi.org/10.1002/mrm.10171>
- Haldar, J.P., Zuo, J., 2016. P-LORAKS: Low-rank modeling of local k-space neighborhoods with parallel imaging data. *Magn. Reson. Med.* 75, 1499–1514. <https://doi.org/10.1002/mrm.25717>
- Hammernik, K., Klatzer, T., Kobler, E., Recht, M.P., Sodickson, D.K., Pock, T., Knoll, F., 2018. Learning a variational network for reconstruction of accelerated MRI data. *Magn. Reson. Med.* 79, 3055–3071. <https://doi.org/10.1002/mrm.26977>
- He, Z., Zhou, J., Liang, D., Wang, Y., Liu, Q., 2019. Learning Priors in High-frequency Domain for Inverse Imaging Reconstruction. <https://doi.org/10.48550/arXiv.1910.11148>
- Huang, J., Fang, Y., Wu, Y., Wu, H., Gao, Z., Li, Y., Ser, J.D., Xia, J., Yang, G., 2022. Swin transformer for fast MRI. *Neurocomputing* 493, 281–304. <https://doi.org/10.1016/j.neucom.2022.04.051>
- Hyun, C.M., Kim, H.P., Lee, S.M., Lee, S., Seo, J.K., 2018. Deep learning for undersampled MRI reconstruction. *Phys. Med. Biol.* 63, 135007. <https://doi.org/10.1088/1361-6560/aac71a>
- Kocanaogullari, D., Eksioglu, E.M., 2019. Deep Learning For Mri Reconstruction Using A Novel Projection Based Cascaded Network, in: 2019 IEEE 29th International Workshop on Machine Learning for Signal Processing (MLSP). Presented at the 2019 IEEE 29th International Workshop on Machine Learning for Signal Processing (MLSP), pp. 1–6. <https://doi.org/10.1109/MLSP.2019.8918715>
- Korkmaz, Y., Dar, S.U., Yurt, M., Özbeý, M., Çukur, T., 2022. Unsupervised MRI Reconstruction via Zero-Shot Learned Adversarial Transformers. *IEEE Trans. Med. Imaging* 1–1. <https://doi.org/10.1109/TMI.2022.3147426>
- Korkmaz, Y., Yurt, M., Dar, S.U.H., Özbeý, M., Cukur, T., 2021. Deep MRI Reconstruction with Generative Vision Transformers, in: Haq, N., Johnson, P., Maier, A., Würfl, T., Yoo, J. (Eds.), Machine Learning for Medical Image Reconstruction, Lecture Notes in Computer Science. Springer International Publishing, Cham, pp. 54–64. https://doi.org/10.1007/978-3-030-88552-6_6
- Liu, X., Yu, H.-F., Dhillon, I., Hsieh, C.-J., 2020. Learning to Encode Position for Transformer with Continuous Dynamical Model, in: Proceedings of the 37th International Conference on Machine Learning. Presented at the International Conference on Machine Learning, PMLR, pp. 6327–6335.
- Liu, Z., Lin, Y., Cao, Y., Hu, H., Wei, Y., Zhang, Z., Lin, S., Guo, B., 2021. Swin Transformer: Hierarchical Vision Transformer using Shifted Windows, in: 2021 IEEE/CVF International Conference on Computer Vision (ICCV). Presented at the 2021 IEEE/CVF International Conference on Computer Vision (ICCV), IEEE, Montreal, QC, Canada, pp. 9992–10002. <https://doi.org/10.1109/ICCV48922.2021.00986>
- Lustig, M., Donoho, D., Pauly, J.M., 2007. Sparse MRI: The application of compressed sensing for rapid MR imaging. *Magn. Reson. Med.* 58, 1182–1195. <https://doi.org/10.1002/mrm.21391>
- Manjón, J.V., Carbonell-Caballero, J., Lull, J.J., García-Martí, G., Martí-Bonmatí, L., Robles, M., 2008. MRI denoising using Non-Local Means. *Med. Image Anal.* 12, 514–523. <https://doi.org/10.1016/j.media.2008.02.004>
- Nguyen-Duc, T., Quan, T.M., Jeong, W.-K., 2019. Frequency-splitting dynamic MRI reconstruction using multi-scale 3D convolutional sparse coding and automatic parameter selection. *Med. Image Anal.* 53, 179–196. <https://doi.org/10.1016/j.media.2019.02.001>

- Nishimura, D.G., 1996. Principles of magnetic resonance imaging. [WWW Document]. URL <http://books.google.com/books?id=uz9BAQAAIAAJ>
- Pawar, K., Chen, Z., Shah, N.J., Egan, Gary.F., 2019. A Deep Learning Framework for Transforming Image Reconstruction Into Pixel Classification. *IEEE Access* 7, 177690–177702. <https://doi.org/10.1109/ACCESS.2019.2959037>
- Pawar, K., Chen, Z., Zhang, J., Shah, N.J., Egan, G.F., 2020. Application of compressed sensing using chirp encoded 3D GRE and MPRAGE sequences. *Int. J. Imaging Syst. Technol.* 30, 592–604. <https://doi.org/10.1002/ima.22401>
- Pawar, K., Egan, G., Zhang, J., 2015. Multichannel Compressive Sensing MRI Using Noiselet Encoding. *PLOS ONE* 10, e0126386. <https://doi.org/10.1371/journal.pone.0126386>
- Pawar, K., Egan, G.F., Chen, Z., 2021. Domain knowledge augmentation of parallel MR image reconstruction using deep learning. *Comput. Med. Imaging Graph.* 92, 101968. <https://doi.org/10.1016/j.compmedimag.2021.101968>
- Pruessmann, K.P., Weiger, M., Scheidegger, M.B., Boesiger, P., 1999. SENSE: Sensitivity encoding for fast MRI. *Magn. Reson. Med.* 42, 952–962. [https://doi.org/10.1002/\(SICI\)1522-2594\(199911\)42:5<952::AID-MRM16>3.0.CO;2-S](https://doi.org/10.1002/(SICI)1522-2594(199911)42:5<952::AID-MRM16>3.0.CO;2-S)
- Ran, M., Xia, W., Huang, Y., Lu, Z., Bao, P., Liu, Y., Sun, H., Zhou, J., Zhang, Y., 2021. MD-Recon-Net: A Parallel Dual-Domain Convolutional Neural Network for Compressed Sensing MRI. *IEEE Trans. Radiat. Plasma Med. Sci.* 5, 120–135. <https://doi.org/10.1109/TRPMS.2020.2991877>
- Ravishankar, S., Bresler, Y., 2011. MR Image Reconstruction From Highly Undersampled k-Space Data by Dictionary Learning. *IEEE Trans. Med. Imaging* 30, 1028–1041. <https://doi.org/10.1109/TMI.2010.2090538>
- Recht, M.P., Zbontar, J., Sodickson, D.K., Knoll, F., Yakubova, N., Sriram, A., Murrell, T., Defazio, A., Rabbat, M., Rybak, L., Kline, M., Ciavarra, G., Alaia, E.F., Samim, M., Walter, W.R., Lin, D.J., Lui, Y.W., Muckley, M., Huang, Z., Johnson, P., Stern, R., Zitnick, C.L., 2020. Using Deep Learning to Accelerate Knee MRI at 3 T: Results of an Interchangeability Study. *AJR Am. J. Roentgenol.* 215, 1421–1429. <https://doi.org/10.2214/AJR.20.23313>
- Robson, M.D., Gore, J.C., Constable, R.T., 1997. Measurement of the point spread function in MRI using constant time imaging. *Magn. Reson. Med.* 38, 733–740. <https://doi.org/10.1002/mrm.1910380509>
- Schlemper, J., Caballero, J., Hajnal, J.V., Price, A., Rueckert, D., 2017. A Deep Cascade of Convolutional Neural Networks for MR Image Reconstruction, in: Niethammer, M., Styner, M., Aylward, S., Zhu, H., Oguz, I., Yap, P.-T., Shen, D. (Eds.), *Information Processing in Medical Imaging, Lecture Notes in Computer Science*. Springer International Publishing, Cham, pp. 647–658. https://doi.org/10.1007/978-3-319-59050-9_51
- Schlemper, J., Caballero, J., Hajnal, J.V., Price, A.N., Rueckert, D., 2018. A Deep Cascade of Convolutional Neural Networks for Dynamic MR Image Reconstruction. *IEEE Trans. Med. Imaging* 37, 491–503. <https://doi.org/10.1109/TMI.2017.2760978>
- Shaw, P., Uszkoreit, J., Vaswani, A., 2018. Self-Attention with Relative Position Representations. *ArXiv180302155 Cs.*
- Sodickson, D.K., Manning, W.J., 1997. Simultaneous acquisition of spatial harmonics (SMASH): Fast imaging with radiofrequency coil arrays. *Magn. Reson. Med.* 38, 591–603. <https://doi.org/10.1002/mrm.1910380414>
- Souza, R., Lebel, R.M., Frayne, R., 2019. A Hybrid, Dual Domain, Cascade of Convolutional Neural Networks for Magnetic Resonance Image Reconstruction, in: *Proceedings of The 2nd International Conference on Medical Imaging with Deep Learning. Presented at the International Conference on Medical Imaging with Deep Learning, PMLR*, pp. 437–446.
- Sun, L., Fan, Z., Ding, X., Cai, C., Huang, Y., Paisley, J., 2019. A divide-and-conquer approach to compressed sensing MRI. *Magn. Reson. Imaging* 63, 37–48. <https://doi.org/10.1016/j.mri.2019.06.014>

- Sung, K., Hargreaves, B.A., 2013. High-frequency subband compressed sensing MRI using quadruplet sampling. *Magn. Reson. Med.* 70, 1306–1318. <https://doi.org/10.1002/mrm.24592>
- Szegedy, C., Wei Liu, Yangqing Jia, Sermanet, P., Reed, S., Anguelov, D., Erhan, D., Vanhoucke, V., Rabinovich, A., 2015. Going deeper with convolutions, in: 2015 IEEE Conference on Computer Vision and Pattern Recognition (CVPR). Presented at the 2015 IEEE Conference on Computer Vision and Pattern Recognition (CVPR), IEEE, Boston, MA, USA, pp. 1–9. <https://doi.org/10.1109/CVPR.2015.7298594>
- Tan, H., Zheng, Y., 2005. Point spread function optimization for MRI reconstruction, in: Proceedings. (ICASSP '05). IEEE International Conference on Acoustics, Speech, and Signal Processing, 2005. Presented at the Proceedings. (ICASSP '05). IEEE International Conference on Acoustics, Speech, and Signal Processing, 2005., p. ii/477-ii/480 Vol. 2. <https://doi.org/10.1109/ICASSP.2005.1415445>
- Valanarasu, J.M.J., Oza, P., Hacihaliloglu, I., Patel, V.M., 2021. Medical Transformer: Gated Axial-Attention for Medical Image Segmentation, in: de Bruijne, M., Cattin, P.C., Cotin, S., Padoy, N., Speidel, S., Zheng, Y., Essert, C. (Eds.), *Medical Image Computing and Computer Assisted Intervention – MICCAI 2021*. Springer International Publishing, Cham, pp. 36–46. https://doi.org/10.1007/978-3-030-87193-2_4
- Vaswani, A., Shazeer, N., Parmar, N., Uszkoreit, J., Jones, L., Gomez, A.N., Kaiser, Ł., Polosukhin, I., 2017. Attention is All you Need, in: *Advances in Neural Information Processing Systems*. Curran Associates, Inc.
- Wachinger, C., Yigitsoy, M., Rijkhorst, E.-J., Navab, N., 2012. Manifold learning for image-based breathing gating in ultrasound and MRI. *Med. Image Anal.* 16, 806–818. <https://doi.org/10.1016/j.media.2011.11.008>
- Wang, S., Su, Z., Ying, L., Peng, X., Zhu, S., Liang, F., Feng, D., Liang, D., 2016. Accelerating magnetic resonance imaging via deep learning, in: 2016 IEEE 13th International Symposium on Biomedical Imaging (ISBI). Presented at the 2016 IEEE 13th International Symposium on Biomedical Imaging (ISBI), pp. 514–517. <https://doi.org/10.1109/ISBI.2016.7493320>
- Wang, S., Xiao, T., Liu, Q., Zheng, H., 2021. Deep learning for fast MR imaging: A review for learning reconstruction from incomplete k-space data. *Biomed. Signal Process. Control* 68, 102579. <https://doi.org/10.1016/j.bspc.2021.102579>
- Weller, D., 2016. Reconstruction with dictionary learning for accelerated parallel magnetic resonance imaging, in: 2016 IEEE Southwest Symposium on Image Analysis and Interpretation (SSIAI). Presented at the 2016 IEEE Southwest Symposium on Image Analysis and Interpretation (SSIAI), pp. 105–108. <https://doi.org/10.1109/SSIAI.2016.7459186>
- Wu, Y.-C., Du, H., Mei, W., 2016. Filter-based compressed sensing MRI reconstruction. *Int. J. Imaging Syst. Technol.* 26, 173–178. <https://doi.org/10.1002/ima.22171>
- Yaman, B., Hosseini, S.A.H., Moeller, S., Ellermann, J., Uğurbil, K., Akçakaya, M., 2020. Self-supervised learning of physics-guided reconstruction neural networks without fully sampled reference data. *Magn. Reson. Med.* 84, 3172–3191. <https://doi.org/10.1002/mrm.28378>
- Yan, C., Shi, G., Wu, Z., 2021. SMIR: A Transformer-Based Model for MRI super-resolution reconstruction, in: 2021 IEEE International Conference on Medical Imaging Physics and Engineering (ICMIPE). Presented at the 2021 IEEE International Conference on Medical Imaging Physics and Engineering (ICMIPE), pp. 1–6. <https://doi.org/10.1109/ICMIPE53131.2021.9698880>
- yang, yan, Sun, J., Li, H., Xu, Z., 2016. Deep ADMM-Net for Compressive Sensing MRI, in: *Advances in Neural Information Processing Systems*. Curran Associates, Inc.
- Yang, G., Yu, S., Dong, H., Slabaugh, G., Dragotti, P.L., Ye, X., Liu, F., Arridge, S., Keegan, J., Guo, Y., Firmin, D., 2018. DAGAN: Deep De-Aliasing Generative Adversarial Networks for Fast Compressed Sensing MRI Reconstruction. *IEEE Trans. Med. Imaging* 37, 1310–1321. <https://doi.org/10.1109/TMI.2017.2785879>

- Yang, Y., Liu, F., Xu, W., Crozier, S., 2015. Compressed Sensing MRI via Two-stage Reconstruction. *IEEE Trans. Biomed. Eng.* 62, 110–118. <https://doi.org/10.1109/TBME.2014.2341621>
- Zbontar, J., Knoll, F., Sriram, A., Murrell, T., Huang, Z., Muckley, M.J., Defazio, A., Stern, R., Johnson, P., Bruno, M., Parente, M., Geras, K.J., Katsnelson, J., Chandarana, H., Zhang, Z., Drozdal, M., Romero, A., Rabbat, M., Vincent, P., Yakubova, N., Pinkerton, J., Wang, D., Owens, E., Zitnick, C.L., Recht, M.P., Sodickson, D.K., Lui, Y.W., 2019. fastMRI: An Open Dataset and Benchmarks for Accelerated MRI. *ArXiv181108839 Phys. Stat.*
- Zheng, H., Fang, F., Zhang, G., 2019. Cascaded Dilated Dense Network with Two-step Data Consistency for MRI Reconstruction, in: *Advances in Neural Information Processing Systems*. Curran Associates, Inc.
- Zhu, B., Liu, J.Z., Cauley, S.F., Rosen, B.R., Rosen, M.S., 2018. Image reconstruction by domain-transform manifold learning. *Nature* 555, 487–492. <https://doi.org/10.1038/nature25988>